Holocene hydroclimate variability along the Southern Patagonian margin (Chile) reconstructed from Cueva Chica speleothems

C. Nehme, D. Todisco, S.F.M. Breitenbach, Isabelle Couchoud, M. Marchegiano, M. Peral, H. Vonhof, J. Hellstrom, R. Tjallingii, P. Claeys, et al.

Holocene hydroclimate variability along the Southern Patagonian margin (Chile) reconstructed from Cueva Chica speleothems

Nehme, Carole; Todisco, Dominique; Breitenbach, Sebastian F.M.; Couchoud, I.; Marchegiano, Marta; Peral, Marion; Vonhof, Hubert; Hellstrom, J.; Tjallingii, R.; Claeys, Philippe; Borrero, L.; Martin, F.

Published in:
Global and Planetary Change

DOI:
10.1016/j.gloplacha.2023.104050

Publication date:
2023

Holocene hydroclimate variability along the Southern Patagonian margin (Chile) reconstructed from Cueva Chica speleothems

Authors: Nehme C.[a,c], Todisco D.[a], Breitenbach S.F.M.[b], Couchoud I.[d], Marchegiano M.[c], Peral M.[c], Vonhof H.[e], Hellstrom J.[f], Tjallingi R.[g], Claeys P.[d], Borrero L.[h], Martin F.[i]

a IDEES UMR 6266 CNRS, University of Rouen-Normandy, France
b Northumbria University, Newcastle upon Tyne, Department of Geography and Environmental Sciences, NE1 8ST, United Kingdom
c Analytical Environmental & Geo-Chemistry, Faculty of Science, Vrije Universiteit Brussel, Belgium
d Environnements, Dynamiques et Territoires de la Montagne, UMR 5204 CNRS, Université de Savoie, Bourget-du-Lac, France
e Max Planck Institute of Chemistry, Hahn-Meitnerweg 1, Mainz, Germany.
f School of Earth Sciences, The University of Melbourne, Melbourne, Australia
g German Research Centre for Geosciences, GFZ 14473, Potsdam, Germany
h Departamento de Investigaciones Prehistoricas y Arqueológicas (CONICET), Universidad de Buenos Aires, Argentina.
i Centro de Estudios del Hombre Austral, Instituto de la Patagonia, Universidad de Magallanes, Punta Arenas, Chile.

1 Introduction

Patagonia is ideally situated to reconstruct past migrations of the Southern westerly winds (SWWs) due to its southerly maritime location. It is the most southerly landmass and is almost surrounded by oceans: the Pacific Ocean to the west, the Atlantic Ocean to the east, the Southern Ocean to the South (Fig. 1). The dominating feature of the Southern mid-high latitudes is prevailing SWWs, which are responsible for driving the circulation of the Southern Ocean, the eastwards Antarctic Circumpolar Current (ACC) and the Peru-Chile Current (PCC) (Lamy et al., 2002, 2015). The SWWs are an important driver of Southern Ocean upwelling (Bakun et al., 2010) and their strength and latitudinal position are predominantly controlled by sea surface temperatures (SST) (Lamy et al., 2010). The SWWs have the strongest velocities between ~50° and 55°S. They seasonally migrate each year in response to the expansion and contraction of the Antarctic Sea ice (Aceituno et al., 1993) and the expansion of the Southern Polar Sea (Garreaud et al., 2013). Nevertheless, the latitudinal position and intensity of the SWWs changed in the past (Fletcher and Moreno, 2011), leading thus to different responses of the vegetation to past climate changes along the Chilean continental margin.

Several paleoenvironmental studies in the last decade showed that the SWWs impacted the climate variability of the Southern Patagonia during the last glacial termination and the Holocene periods (Moreno et al., 2012; 2018a, Zolitschka et al., 2019) as a consequence of deglaciation and long-term SST changes (Lamy et al., 2010, Shevenell et al., 2011, Ivanovic et al., 2018) in the South Pacific Ocean. This led to different environmental responses of ecosystems (Mansilla et al., 2016; 2018, McCulloch et al., 2001; 2019; 2020; 2021) to past climate change throughout the Chilean landmass, with records showing periods of warmer climate when the SWWs shifted poleward and cooler climate, when the SWWs shifted equatorward (Toggweiler et al., 2006). The westerlies' pattern and fluctuations even increased since the mid-Holocene along with higher SST gradients, leading to rapid climate cycles (RCC) recorded in some derived-pollen data from lacustrine records (Moreno et al., 2016, 2018b).

Whether long- or short-term changes in the SWWs were recorded in the Patagonian records, the sensitivity of such terrestrial records depends on gradients including the latitudinal position, distance to the coast as well as exposure to SWWs. In the complex geographical settings of Patagonia, a dissimilar distribution of rainfall is noticeable: orographic precipitation is produced as the SWWs reach the western coast and are driven upwards over the Andean Cordillera leading to a hyper-humid region in the west (~8000 mm/a) with the moisture decreasing eastwards, creating a rain shadow effect (~500 mm/a) (Schneider et al., 2003). This East-West precipitation gradient is reflected nowadays in the ecotones that range from Moorland and Evergreen Forest in the west to Steppic open field landscape in the east (Tuhkanen et al., 1990).

Among the various lacustrine (Moreno et al., 2018a, 2019; Zolitschka et al., 2019), peat (Mansilla et al., 2016, 2018; McCulloch et al., 2020, 2021) and soil (Alloway et al., 2017) records that helped reconstruct the vegetation history and their climatic feedback in Southern Patagonia, very few are based on the study of geochemical proxies directly linked to the hydroclimate variability of rainfall or temperature. The only two geochemical proxy-based records from carbonates (Solari et al., 2010; Schimpf et al., 2011) are discontinuous and span only the late-Holocene period. Speleothems (e.g., stalagmites, flowstone) are secondary chemical carbonates deposited in caves and represent the most suitable terrestrial archives for establishing high resolution proxy time-series in paleoclimate research (Genty et al., 2003; Cheng et al., 2012; Fairchild and Baker, 2012). Beyond qualitative trends provided by the isotopic signature and trace-

elements trapped in their laminae, speleothems can also provide quantitative estimates of paleoclimate data (e.g. temperature, rainfall amount) either through cave-specific proxy calibration (Tremaine et al., 2011) or through the isotopic analysis of fluid inclusions trapped within the carbonate speleothems at the time of their formation (van Breukelen et al, 2008; Matthews et al., 2021; Wassenburg et al., 2021). Moreover, the application of clumped isotopes on associated calcite (Eiler 2007; 2011) provides an additional control on the cave temperature and its variation at the time of speleothem formation (Affek et al., 2008; Matthews et al., 2021).

This study presents a new flowstone core S6-S6bis and a stalagmite S8 from The Cueva Chica located in the south-eastern part of the Cerro Benitez (S51°33'; W 72°33'), Ultima Esperanza region in Patagonia, Chile. A series of radiometric dating, petrographical and geochemical analyses (stables isotopes, chemical composition), combined with monitoring data of the cave was conducted to produce trace elements and isotope time-series. The Chica speleothems provide a high-resolution and well-dated terrestrial record spanning the hydroclimate history of the Southern Patagonia for the last 12 ka BP. We evaluate the timing and intensity of past climatic change throughout the Holocene and discuss both in conjunction with available marine and regional paleoenvironmental records in order to better constrain the regional paleoclimatic evolutions of SWWs. Lower resolved quantitative temperatures estimates are combined with higher resolved proxies to bolster our qualitative paleoclimatic reconstructions.

2 Environmental settings of Cerro Benitez and Chica cave

Cerro Benitez, a small hill of 520 m a.s.l., is located 20 km north of Puerto Natales, in the Eastern Andes, 10 km inland from the East coast of the Última Esperanza fjord (Fig. 1). The hill is comprised of conglomerates of the Cerro Toro formation (Romans et al., 2011), smoothed by successive glacial advances draining the South-Eastern part of the South Patagonian icefield. An East-West running glacial valley, today partially occupied by Lago (lake) Sofía, borders the Northern flanks of Cerro Benítez. Lago Sofia is the remnant of a large ice-dammed proglacial lake (proglacial Lago Puerto Consuelo) formed after the glacier retreated around 17.5 ka (Sagredo et al., 2011; Stern et al., 2011). The hill is surrounded by late Pleistocene erosional platforms and palaeoshorelines (Girault et al., 2022).

Cerro Benitez is influenced by the SWWs, which deliver precipitation from the Southeast Pacific (Fig. 1). The nearest meteorological station at Puerto Natales (51°44′S, 72°31′W, 2 m a.s.l.) receives 513 mm precipitation annually, which are well distributed through the whole year. Precipitation maxima occur in March, April, August, and November. The mean annual air temperature (MAAT) is between 6° and 7°C with an annual range of 9°–10°C (Dirección Meteorológica de Chile, www.meteochile.gob.cl/inicio.php). The limited moisture compared to the Western side of the Andes, results in a distinct forest-steppe ecotone covering the Eastern slope of the mountains, and particularly Cerro Benitez (Villa-Martínez and Moreno 2007; Moreno et al., 2009).

In the Southern flanks of Cerro Beníte, a few meters above the late Pleistocene 155 m asl lake terrace, a series of caves and rock shelters were partially sediment filled. This infilling occurred after several glacier retreats and advances from 30 ka to 18 ka BP (Girault et al., 2022). More than thirteen underground galleries comprise fossil remnants of megafauna in cave deposits (Villavicencio et al., 2016), which today comprise the oldest paleontological and archaeological material in the region (Prieto, 1991; Nami and Nakamura, 1995; Borrero and Franco, 1997; Martin et al., 2015; Martin and Borrero 2017). Two caves (Cave Lago Sofía 1 and el Medio Cave) feature two of the oldest archaeological records of Patagonia, dated between 13.6 and 10.6 ka cal. BP, while Chica Cave features the oldest paleontological record of the region, a *Lama gracilis* astragale dated to 18.500-17.930 cal. BP.

Chica Cave (S51°34'23.55"; W72°35'8.09") opens at 162 m a.s.l. and develops in complex mudstone/sandstone strata of the Cerro Torro formation. With its 73 m long relict conduits Chica cave is the most karstified site studied here. The cave is characterized by phreatic morphologies as well as unconsolidated and laminated sediments that are partially sealed with a thick calcite flowstone (Suppl., fig. 1). Seasonal drip and meteoric water flow on flowstone is still active in the Eastern gallery. As no stalagmites are preserved in the cave due to vandalism, a 40x6 (Lxl) cm core "S6" and a 5x5 (Lxl) cm core "S6bis" were retrieved from the flowstone at the end of the Western gallery (Suppl., fig.1). Additionally, a broken stalagmite (sample "S8") has been collected on site. Temperature loggers placed both outside and inside the cave between December 2018 and December 2019, show an average temperature of 4.6 ± 0.6°C inside the

cave and 9.4°C outside in summer and 2°C in winter (Suppl., fig. 2). The catchment area of the cave comprises hilly slopes covered by scattered trees of Nothofagus. Some areas are covered by open grassland and peat vegetation. It is noteworthy that the catchment of the cave is downstream the Vega Benitez peat bog (McCulloch et al., 2021).

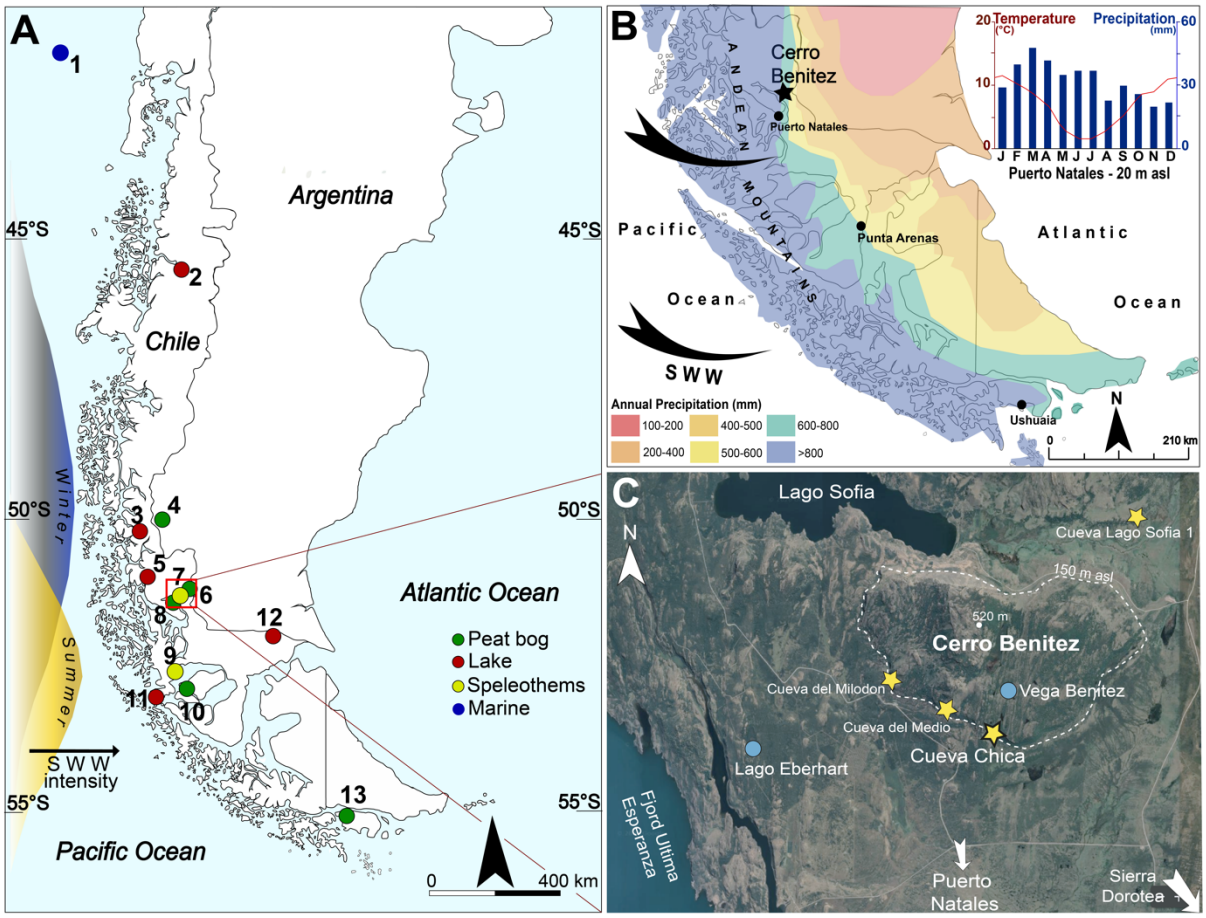

Fig. 1*. Overview of southernmost Chile with the study site.* ***A)*** *Map of southernmost Chile with sites of discussed paleoclimate records: 1 – Marine cores GeoB3313-1 (Lamy et al., 2002) and ODP1233 (Lamy et al., 2015), 2 – lake Mallin Pollux (Markgraf et al., 2007), 3 - Lago Argentino (Kaplan et al., 2016), 4 - Cerro Frias peat (Tonello et al., 2009), 5 - Lago Cipreses (Moreno et al., 2018), 6 - Vega Benitez peat (McCulloch et al., 2021), 7 -* ***Chica cave*** *(this study), 8 - Lago Eberhart peat (Moreno et al., 2012), 9 – Marcelo Arevalo (MA) cave (Schimpf et al., 2011), 10 - GC peat bog (Killian et al., 2003; Lamy et al., 2010), 11 - lake Tamar (Lamy et al., 2010), 12 - lake Potrok Aike (Schäbitz et al., 2013), 13 - Pta Burselem & Isla Navarino peats (McCulloch et al., 2019; 2020). Latitudinal changes of average westerly wind intensities in summer and winter between 1960 & 2000 AD are shown in yellow and blue (source: NCEP-NCAR).* ***B)*** *Annual precipitation over southernmost Chile (Schneider et al., 2003). Insert shows an ombrothermal diagram of Puerto Natales (www.climate-data.org).* ***C)*** *Study area Cerro Benitez with caves (yellow stars) and peatbogs (blue circles) mentioned in this study.*

3 Methods

3.1. Petrography

Both S6 and S6bis cores and stalagmite S8 were cut along their growth axes, polished using 120–4000 µm silicon carbide sandpaper. Twelve thin sections (80-100 µm thick) were prepared at the department for Sediment and Isotope Geology, Ruhr University Bochum, Germany. A petrographic analysis was conducted with a Leica optical microscope to determine the stratigraphical characteristics of core S6 (e.g., fabrics, structures, inclusions, discontinuities, hiatuses).

3.2. U-series and ^{14}C dating

Seventeen samples of between 30 and 230 mg were extracted from the sectioned cores S6 and S6bis and stalagmites S8 for U/Th dating using 0.5 to 0.8 mm tungsten carbide dental bits mounted on a Sherline 2010 micromill. Samples were dissolved in isolation using 1.5M HNO_3, spiked with a measured quantity of ^{233}U-^{229}Th or ^{236}U-^{233}U-^{229}Th mixed synthetic isotopic tracer (Hellstrom, 2003; Drysdale et al., 2012) and allowed

to equilibrate on a hotplate overnight. U and Th were separated from the carbonate matrix using Eichrom TRU ion exchange resin and established methods (Luo et al, 1997), modified to collect U and Th in the same fraction using 0.1M HCl–0.2M HF (Hellstrom, 2003). Mass spectrometric analysis was undertaken at the University of Melbourne using either a Nu Instruments Plasma MC-ICP-MS with standard collector block or a similar instrument with modified collector block placing simultaneously using the high- and low-mass SEM ion counters in each case (Hellstrom, 2003). Ion counter gain was determined using ion counter and Faraday measurements of ^{235}U and ^{229}Th for the standard collector block and $^{236}U/^{233}U$ and ^{229}Th for the modified collector bloc mass bias was determined using the bulk earth natural $^{238}U/^{235}U$ ratio of 137.88, this technique being relatively insensitive to error in this ratio due to the simultaneous measurement of $^{229}Th/^{230}Th$ and $^{233}U/^{234}U$. Ion counter baselines were measured at half mass units and interpolated for ^{234}U and ^{230}Th. Initial $^{230}Th/^{232}Th$ activities were determined by stratigraphic constraint (Hellstrom, 2006) where possible, giving a value of 0.93 ± 0.08.

An additional ^{14}C date was obtained through the analysis of 10 mg of charcoal sampled on core S6bis. The preparation and measurement were completed at the Radiochronology lab from Laval University, Québec, Canada. Radiocarbon concentrations are given as fractions of the modern standard, $\delta^{14}C$, and conventional radiocarbon age, following the conventions of Stuiver and Polach (1977). Result was corrected for isotope fractionation according to the conventions of Stuiver and Polach (1977), with $\delta^{13}C$ value measured on the graphite prepared, using the AMS spectrometer. Stratigraphic correspondence (Suppl., fig. 3) combined with U-Th dates from core S6bis permits the inclusion of the radiocarbon date into the age model, after the calibration (cal. BP) of the measured age (Suppl., fig. 5), using OxCal program (Bronk Ramsey, 2009) and the atmospheric data from Reimer et al. (2020).

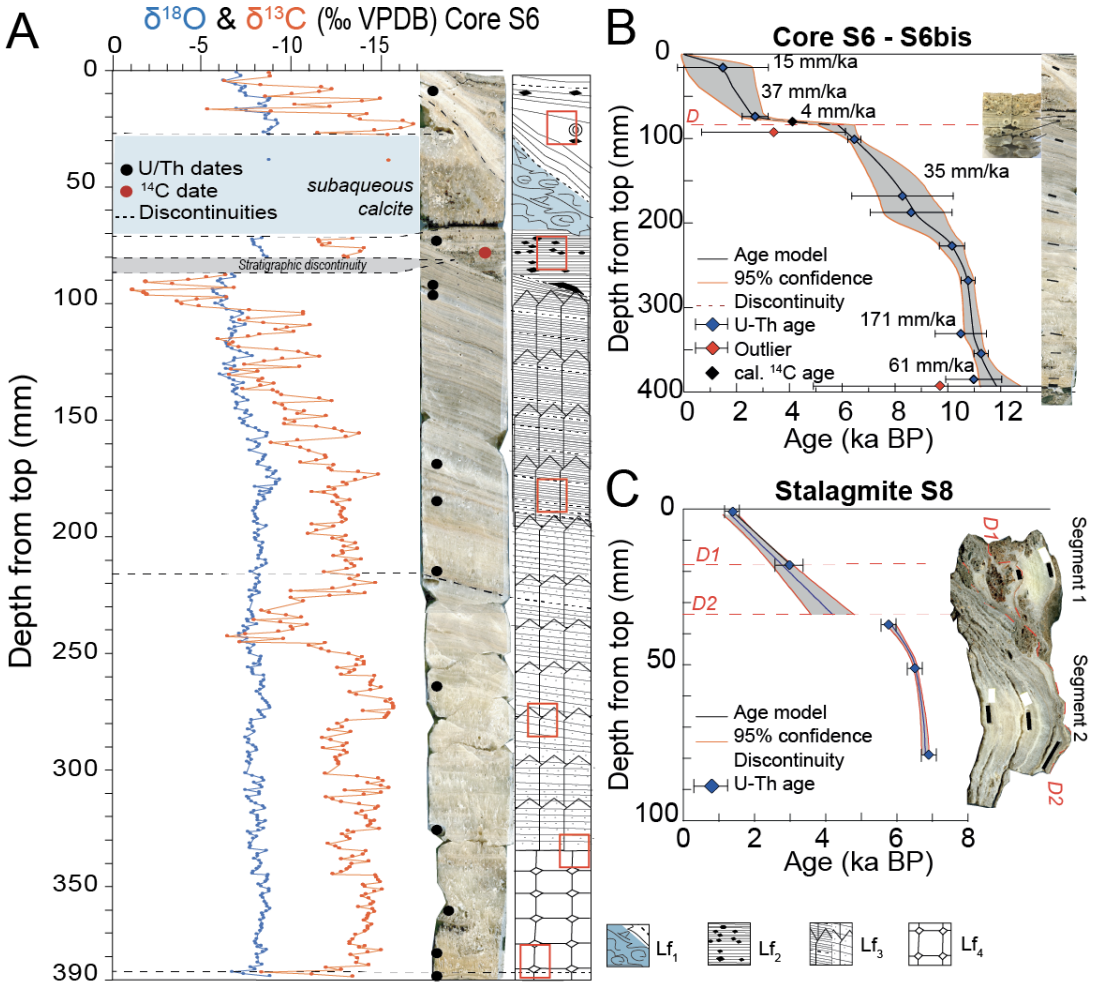

***Fig. 2**. Lithofacies, stable isotope and age models for the studied samples. **A.** Stable isotope depth profile along the S6 core together with U/Th and ^{14}C dates and lithofacies. Explanation of lithofacies and red rectangles locating the thin sections are displayed in the supplementary (Suppl. S2). **B**. Age-depth model of core S6 and S6bis. **C**. Age-depth model for stalagmite S8. Age-depth models are based on COPRA (Breitenbach et al., 2012).*

3.3. Calcite and water stable isotopes measurements

Stable isotope samples were taken along the growth axis of core S6 and stalagmite S8 (Fig. 2) for $\delta^{13}C$ and $\delta^{18}O$ measurements. Overall, 310 samples were measured in core S6 and 68 in stalagmite S8. Samples were drilled along the stalagmite growth axis at 1 mm resolution using a Merchantek Micromill mounted on a Leica microscope. Between every sample, the drill bit and sampling surface were cleaned with compressed air. In addition, two recent calcite samples underneath active drip water were collected nearby the sampling area and measured for $\delta^{13}C$ and $\delta^{18}O$. The samples were analysed using a Nu Carb carbonate device coupled to a Nu Perspective mass spectrometer (MS) at the Vrije Universiteit Brussel, Belgium. Part of the samples were measured at the Sediment and Isotope Geology department, Ruhr University Bochum, Germany, using a Thermo Gasbench II connected to a Thermo MAT253 Plus MS in continuous flow mode. All $\delta^{18}O$ and $\delta^{13}C$ values are calibrated against Vienna Pee-Dee Belemnite (V-PDB) and are reported in permil (‰). Analytical uncertainties were better than 0.1 ‰ (1σ) for oxygen and 0.05 ‰ (1σ) for carbon on both instruments.

Sixteen water samples were collected from the Cueva Chica and nearby caves, springs and lakes in December 2016, 2017, and 2018 for $\delta^{18}O$ and δD measurements in hermetically sealed glass bottles. Isotope measurements were performed at the Vrije Universiteit Brussel on a Picarro L2130-i analyzer using the cavity ring-down spectroscopy (CRDS) technique (Van Geldern and Barth Johannes, 2012). All values are reported in permil relative to Vienna Standard Mean Ocean Water (VSMOW). Analytical uncertainties (1σ) were better than 1 ‰ for δD and 0.1 ‰ for $\delta^{18}O$.

3.4. µXRF element data

The elemental distribution of Ca and Sr has been determined in core S6 using a µX-ray fluorescence (µXRF) scanning. The scanning maps were selected along the stable isotope track using an Bruker M4 Tornado µXRF spectrometer at the GFZ (Potsdam, Germany). The µXRF is equipped with a 50W Rh X-ray source that was operated at 50 kV and 600 µA with a spot sizer of 20 µm. Measurements were performed under vacuum every 50 µm and a counting time of 25 ms. The resulting element intensities are given in counts per second (cps) and Sr element intensities were normalized over Ca to minimize sample density effects. The Sr/Ca ratios were scaled by multiplying the intensity ratios by 1000, and transferred on to the age scale though the age–depth model.

3.5. Fluid inclusions stable isotope (H-O) analyses

Fluid inclusion δD and $\delta^{18}O$ values from core S6 were obtained at the Max Planck Institute for Chemistry in Mainz, Germany. Nine samples, consisting of 1 to 2 chips (Suppl., fig.7) weighing in total 0.6-0.8 g were placed in a crushing cell and pre-heated at 115°C in a moisturized nitrogen flow for 20 minutes before crushing. Liberated fluid inclusion water was analysed in a Picarro 2140i analyser. The contribution of the ~13000 ppm water background in the N2 carrier gas, which serves to remove sample-to-sample memory effects in this analytical system, is mathematically subtracted from the isotope values analysed for the crushed sample (Affolter et al 2014; De Graaf et al., 2020). A detailed description of the analytical technique as it is set up at MPIC can be found in De Graaf et al. (2020). The Cueva Chica data were collected in two different series. For each series more than10 aliquots of standard water were injected in the crusher system, analysed identically to the crushed samples and reproduced within 0.09 ‰ for $\delta^{18}O$ and 0.3 ‰ for δD for both series (1σ). All fluid inclusion isotope data are reported on the VSMOW2-SLAP2 scale.

3.6. Clumped isotopes

Clumped isotope analyses were carried out at the AMGC laboratory of Vrije Universiteit Brussel (VUB), Belgium, using a Nu-Pespective-IS-IRMS combined with a Nu-Carb system. The full methodology for the Δ_{47} analyses performed at the AMGC-VUB lab is described in De Vleeschouwer et al. (2022). A total of seven samples (Suppl., fig.7) from core S6 were analysed and replicated 10 to 15 times (Suppl., table 2). For each analysis, a minimum of 500 µg of carbonate was reacted at 70°C with H_3PO_4 acid. Possible contaminations were tracked by scrutinising raw Δ_{49} values of ETH1-4 standards for significant deviations from the mean (Meckler et al., 2014). ETH standards were measured following the recommendations of Kocken et al. (2019) with a sample to standard ratio of 1:1. Analyses were constantly monitored using the Easotope software (John and Bowen, 2016). The raw Δ_{47} values were processed using the IUPAC isotopic parameters (Brand et al., 2010; Daëron et al., 2016; Petersen et al., 2019) within the ClumpyCrunch software (Daëron, 2021) and converted to the I-CDES 90°C scale (Bernasconi et al., 2021). The Δ_{47} values were converted to temperatures using the regression of Anderson et al. (2021). Temperature uncertainties were calculated by propagating the standard error (SE) for each sample and the uncertainties associated with the

calibration. The Δ_{47} uncertainties (SE) are based on external Δ_{47} reproducibility of our analytical sessions of measurements, based on repeated analyses of standards and samples.

4 Results

4.1. Petrography

Petrographic analysis of thin sections (Suppl., fig. 2) shows that core S6 is mainly composed of columnar calcite, which ranges from poorly-to-well laminated to massive, often with a persistent component of detrital impurities. Based on clastic content, fabrics, and colour of the calcite, four main lithofacies are identified in core S6. From base to top (Fig. 2) we observe:

i) Lithofacies Lf_4, from 392 to 335 mm from top, rich in clastic material and characterised by yellowish calcite with poorly laminated and more porous structure embedded in a micro-gour structure. Lf_4 reveals a low but significant content of oxides, rutile and microcalcite fragments (e.g., micrite, sparite) filling the voids between the calcite crystals.

ii) Lithofacies Lf_3, from 335 to 98 mm, composed of compact, elongated columnar calcite with highly laminated structure. Few empty voids are found compared to Lf_4. While the basal part of Lf_3 shows few impurities and more, well recognizable, fluid inclusions, the upper part shows more impurities and a higher number of hiatuses.

iii) Lithofacies Lf_2, from 98 to 50 mm, less clearly laminated but comprises the highest number of impurities, minerals, bones fragments (microfaunal), and remains of organic material (e.g. amorph material, unidentified plant remains in the entire record. Oxides, rutiles and pyroclasts are the most common identified features.

iv) Lithofacies Lf_1, from 50 mm to the top of the core reveals two kind of microstructures: it is poorly laminated in its upper part with few impurities whereas its lower part shows a primary calcite formed in a subaqueous environment.

4.2. Chronology

Ten uranium-thorium (U/Th) ages were obtained from S6, two dates from S6bis cores and five from stalagmite S8 (Suppl., table 1). Two dates were considered as outliers. Minor age inversions with large uncertainties coincide petrographically with growth intervals rich in detrital material in the flowstone cores (Suppl., fig 3, table 1). High initial thorium concentrations are most likely due to organic material, or iron oxides that are common at depths 390-370 mm and 90-70 mm in core S6. The corresponding dates S6-19-10 and S6bis-01 are out of sequence and were therefore excluded from the age model (Suppl., table 1). The COPRA age-depth model indicates that core S6 grew from *ca.* 11.1 ± 1 to 1.5 ± 1.7 ka BP, including several short discontinuities (Fig. 2B). One noteworthy discontinuity at 80 mm depth in core S6 shows a change in growth (water flow) direction, followed by precipitation of impurities-rich calcite. This discontinuity covers the period from ~5.8 to ~2.7 ka BP. Considering that a thin water film is still running today over the wet flowstone, the age model was bound with the year of sampling in its youngest part. Core S6bis, sampled 10 cm from core S6, grew between 3.4 ± 2.7 ka and 2.7 ± 0.5 ka BP, with a charcoal encrusted in the calcite and dated at 4.11± 0.04 cal BP. Stalagmite S8 grew from 6.8 ± 0.1 to 1.29 ± 0.22 ka BP (Fig. 2B) and a hiatus is observed between 5.7 and 4.2 ka BP. A series of dark detrital layers filled with microfaunal bone fragments mark two major discontinuities, D1 at 18 mm and D2 at 22 mm depth. The latter separates segment 1, dated to between ~4.2 and ~1.3 ka BP, from segment 2, dated to between ~6.7 ka and ~5.7 ka BP.

4.3. Stable isotopic composition of calcite, modern water and fluid inclusions

Stalagmite core S6 $\delta^{18}O$ (-6.28 to -9.81 ‰) and $\delta^{13}C$ (-2.14 to -16.26 ‰) values display distinct signatures (Fig. 3). Between ~12 and ~8.5 ka BP, the time series shows overall low $\delta^{18}O$ values, with the lowest observed at ~8.5 ka BP. A distinct positive excursion is noticeable between 10.5 and 10.1 ka BP. From 8.5 to 6 ka BP, we find a general increase in both $\delta^{18}O$ and $\delta^{13}C$ values and higher multi-decadal scale variability (Fig. 3). The highest isotope values (-6.3 ‰ for $\delta^{18}O$, -2 ‰ for $\delta^{13}C$) are found at ~6 ka BP. From 3.5 to 1.5 ka BP, a shift to lower carbon and oxygen isotope values in core S6 corresponds well with stable isotope profile from stalagmite S8 (Fig.3). After 1.5 ka BP, the upper part of core S6 shows an increase in both the $\delta^{18}O$ and $\delta^{13}C$ values until the present day. The overall resolution of the isotope record is infra- to multi-decadal, except for the topmost part (from ~3.2 to present), which is lower resolved. At a decadal scale, the $\delta^{13}C$ profile co-varies with the $\delta^{18}O$ record. High growth rate (Fig. 2) generally corresponds with lower $\delta^{18}O$ and $\delta^{13}C$ values. After ~8.5 ka BP, the growth rate decreases (Fig. 2B) drastically until ~5.8 ka BP, coeval with a slowly increasing trend in $\delta^{18}O$ and $\delta^{13}C$.

Dripwater stable isotopes collected in the Cueva Chica show an average $\delta^{18}O$ value of -11.24 ‰ and a δD of -91.23 ‰. The isotope values cluster very narrowly and fall at the lower end of, and parallel to, the local meteoric water line (LMWL) (Fig. 4). The corresponding recent calcite deposits that form from the sampled dripwater show a $\delta^{18}O$ value of -7.05 ‰ and $\delta^{13}C$ of -15.2 ‰. Stable isotopes from fluid inclusion exhibit a wide (20 ‰) range of $\delta^{18}O_{FI}$ values, which is much larger than the $\delta^{18}O$ range in the host calcite (3.5 ‰).

The fluid inclusion deuterium isotope ratios (δD_{FI}) data show a 30 ‰ range. In δD – $\delta^{18}O$ space the lowest observed isotope ratios are found close to the GMWL, while values progressively depart from the GMWL following a slope of ~1.4 (Fig. 4).

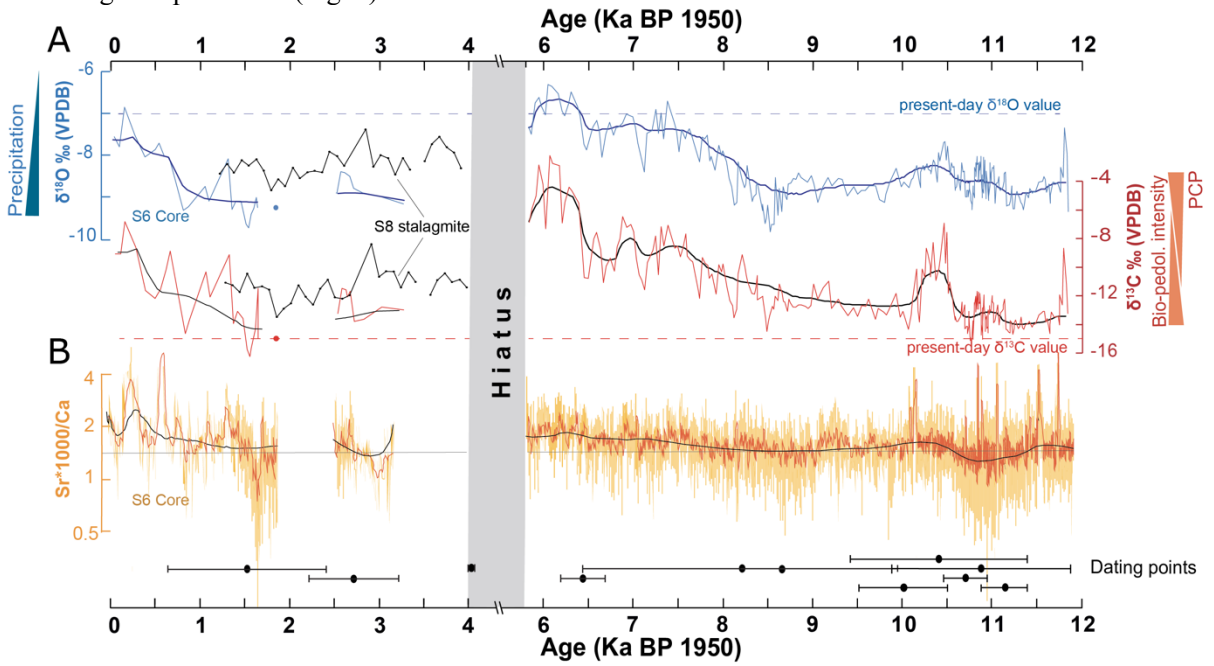

***Fig. 3**. Multiproxy ($\delta^{18}O$, $\delta^{13}C$ and Sr/Ca ratios) records from samples S6 and S8. **A**. The original isotope. **B.** Ratio of µXRF Sr and Ca instenisties (cps) presented as median values (red smoothed line) to highlight the broader trends and variations from 12 ka BP to present. The moving average (black lines) is shown for both stable isotope and Sr/Ca profiles. No Sr/Ca data is available for the periods from 5.5 to 3.2 ka BP, and 2.5 to 2 ka BP.*

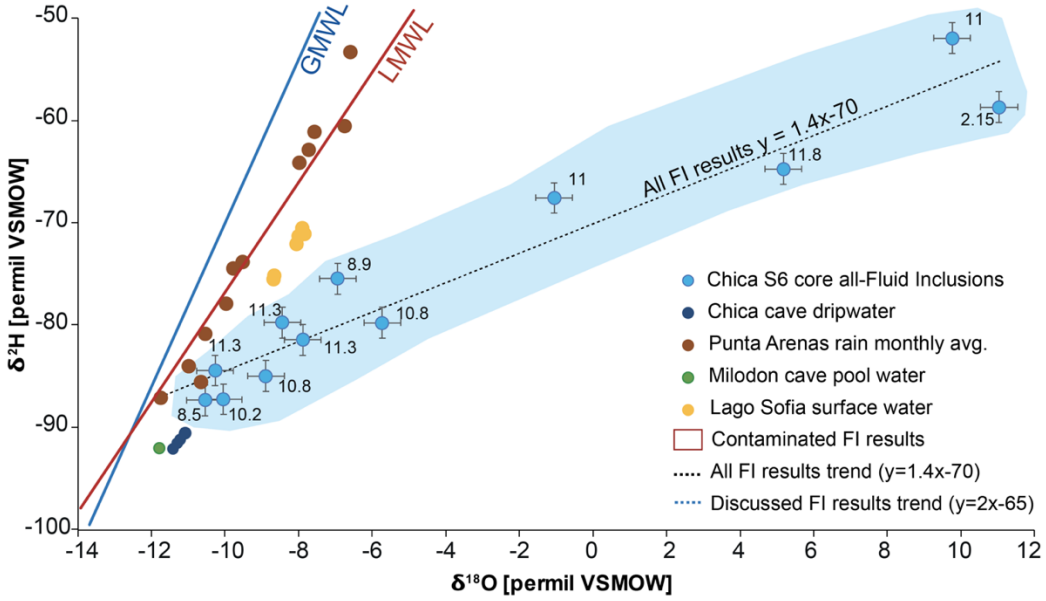

***Fig. 4**. Results of $\delta^{18}O$ and $\delta^{2}H$ analyses of 12 fluid inclusion (FI) samples from core S6 along with modern cave pool, dripwater, river and nearby Lago Sofia (this study) as well as rainwater (IAEA/WMO, 2019) of the nearest monitored station in Punta Arenas, plotted together with the LMWL and GMWL (Rozanski et al., 1993). The age of each FI sample is indicated in the graph and the SE for each FI is better than 0.1 ‰ for $\delta^{18}O$ and 0.3 ‰ for $\delta^{2}H$ (1σ). The FI distribution shows the most contaminated/dirty samples on the right while clean (in terms of detrital content) samples to the left.*

4.4 High resolution Sr/Ca data

The Sr/Ca record of core S6 has a temporal resolution of about 0.1 to 12 years (Fig. 3). The 1000*Sr/Ca ratio varies between 0.2 and 325 cps (avg = 2). The median record (shown in red) varies only little between 1.3 and 2.6 cps but reveals some maxima between prior to 11,5 ka, from ~10,5 and 10 ka BP and from ~1.0 to present-time ka. Minima occur from ~10.8 to 11.5, ~1.8 and ~3 ka BP. From ~12 to 11.4 ka BP, Sr/Ca values are higher (median ~1.6) followed by a peak of lower values from ~11.3 to 10.6 ka BP (median ~1.3). A return to higher values is marked at 10.2 ka and from 9.6 to 9.2 ka BP, followed by a general trend of increased Sr/Ca values (median ~1.6) from ~8.5 to 5.8 ka BP (median from ~1.5 to 1.9), which coincides with high stable isotope values. From 3.2 ka BP onwards, the Sr/Ca median values are low (from ~1.4 to 1.5), except for a short excursion at 0.7 and 0.3 ka BP. More rapid changes in the Sr/Ca ratios (median), showing annual to multi-annual variations, are superimposed on this long-term trend (as shown by the moving average). The Sr/Ca and stable isotope time series vary simultaneously, with higher Sr/Ca values corresponding with more positive $\delta^{18}O$ and $\delta^{13}C$ values.

4.5. Clumped isotope values

The Δ_{47} values of the 8 analyzed samples range from 0.6172 to 0.6601 ‰ (Suppl., table 4). From the bottom to the top (older to younger part of the speleothems), the Δ_{47} values progressively decrease from 0.6528 to 0.6438 ‰ between 11.3 and 6.5 ka BP. The minimum Δ_{47} value is reached with sample C3 at 6.5 ka BP. At the top of the speleothem, both samples C2 and C1 record the highest Δ_{47} value, 0.6601 and 0.6565 ‰ respectively. The sample C0, taken at the top of the speleothem, includes the most recent calcite and records a Δ_{47} value of 0.6415 ‰.

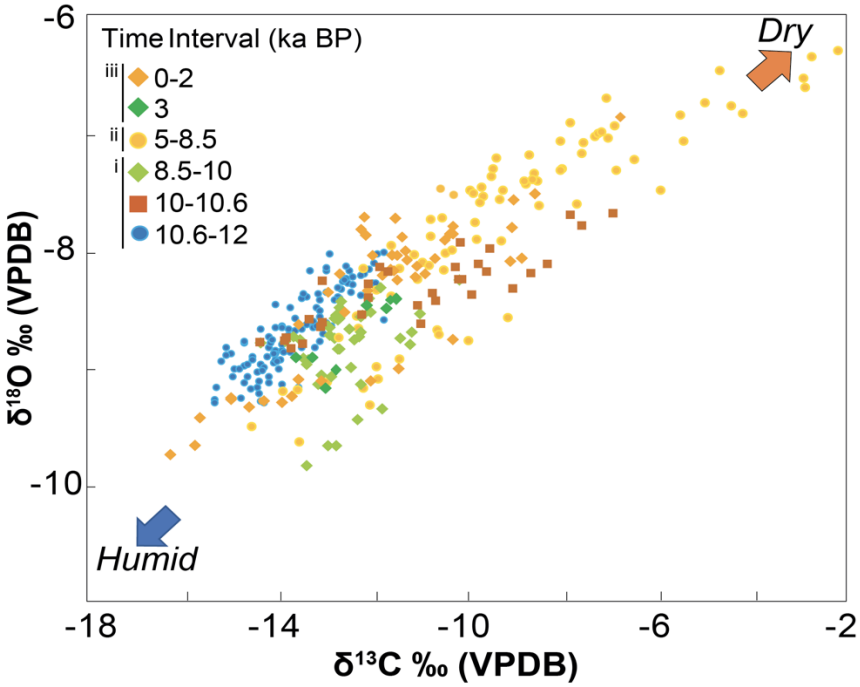

Fig. 5*. Stable oxygen and carbon isotope variability over time, showing their dispersion and interrelationship for different time intervals. Three phases are identified : i) low $\delta^{13}C$ (avg: ~ -15 ‰) and $\delta^{18}O$ values (avg. ~ -9 ‰) during the early-Holocene wet period (with exception of two excursions at 10.5 ka and 8.5 ka), ii) high $\delta^{13}C$ (avg. ~ -8 ‰) and $\delta^{18}O$ values (avg. ~ -7 ‰) during the mid-Holocene dry period, iii) general wet conditions in the late Holocene with low $\delta^{13}C$ (avg. ~ -12 ‰) and $\delta^{18}O$ values (avg. ~ -8 ‰).*

5 Discussion

5.1 Age growth behaviour of the studied speleothems

Building a composite COPRA age-depth models for cores S6a and nearby S6bis required lithofacies comparison of each core under optical microscope for the same depth interval. Optical observation allowed to relate several stratigraphical levels along with an additional ^{14}C dating on charcoal in core S6bis (Suppl., fig., 3) and consider all the ages of core S6 and S6-bis on the same depth profile. The age model for core S6-S6bis (Fig. 2) reveals a rather continuous deposition from ~11.9 to ~5.8 ka BP, with an average growth rate of 90 mm/ka (range 4-300 mm/ka). The basal part from ~12 to ~9 ka BP shows a high growth rate of 170

mm/ka at the beginning of calcite precipitation in the cave. From ~9 ka onwards, the growth rate decreases and remains at/or below 37 mm/ka until ~5.8 ka BP, showing an overall gradual decrease in water availability to build the flowstone. At ~5.8 ka BP, a stratigraphical discontinuity (D) is found, likely resulting from a change in flow direction of the source water. This core section either precipitated at very slow growth rates of 4 mm/ka or contains multiple (unresolved) hiatuses. Charcoal fragments encrusted between clean and muddy calcite layers within D, dates to 4.11± 0.04 cal. BP and could be the result of an enhanced incave water flow event after a vegetation fire (with soil surface erosion by overland flow). The speleothem record continues at 2.7 ± 0.5 ka BP and calcite formed continuously but slowly until the present time, resulting of less favourable conditions for intensive calcite precipitation.

Stalagmite S8 grew from ~6.8 to 2 ka BP, with an average growth rate of 68 mm/ka. A period of apparently very slow growth between 5.8 and 4 ka BP is attributed to either significant drying or one or more hiatuses that remain unresolved with the current dating information. This period of limited growth in stalagmite S8 coincides with the timing of the stratigraphical hiatus in core S6. This and less negative $\delta^{13}C$ and $\delta^{18}O$ values at the time (Fig. 4) signify reduced infiltration and less favourable conditions for intensive calcite precipitation in the cave. Local pollen data confirms our interpretation of drier conditions at the time (McCulloch et al., 2021).

5.2 Interpreting the geochemical proxy record from the Cueva Chica

Stable isotope data from speleothem have been intensively studied in moderate temprate regions (Baldini et al. 2021, McDermott, 2004; Mangini et al., 2005; Lachniet, 2009; Fairchild and Baker, 2012), but less in cold temperate areas such as Patagonia (Schimpf et al., 2011).

5.2.1. $\delta^{13}C$ as proxy for vegetation and soil development

Stalagmite $\delta^{13}C$ can serve as qualitative proxy for changes in vegetation composition and density, soil microbial activity, and, frequently, for changes in infiltration dynamics (Lechleitner et al., 2018; Fohlmeister et al. 2011). At the Cueva Chica, soil and vegetation activity are highest at the end of spring (Nov-Dec). Together with higher effective infiltration during the winter-spring period, this results in higher CO_2 concentrations with low $\delta^{13}C$ signature in the soil. Passing through the epikarst, the $\delta^{13}C$ signal is adjusted to higher values, depending on the residence time of the percolating water and length of water-rock interaction (Lechleitner et al., 2018). In addition, CO_2 degassing can occur i) in the epikarst if air pockets exist in the dry season, leading to prior carbonate precipitation or ii), in a ventilated cave atmosphere (Deininger et al., 2012), in both cases contributing to a shift of $\delta^{13}C$ towards higher values. The speleothems from the Cueva Chica thus record the combined signal of epikarst and in-cave CO_2 degassing, vegetation composition and density as well as soil microbial activity (McDermott, 2004). The observed very low $\delta^{13}C$ values in the Chica record, reaching values such as −16 ‰, corroborate the interpretation that multiple processes, including microbial and plant activity, influence the $\delta^{13}C$ signal. In South Patagonia, the vegetation type is dominantly a C3 type in a broad-leaved forest cover, sometimes mixed with C4 type in open grassland (Cerling and Quade, 1993). Today the Cerro Benitez is covered with *Juncaceae* (rushes) and grasses mixed with sparse forest on thin soils, and several fires have been recorded throughout the Holocene (McCulloch et al., 2021). Thus, the $\delta^{13}C$ signal of postglacial soils above the cave is expected to be much higher than that of a developed *Nothofagus* forest soil ($\delta^{13}C$: -26 ‰ in Peri et al., 2012). More open vegetation or thin soils with limited microbial activity and soil CO_2 production would lead to higher $\delta^{13}C$ (Scholz et al., 2012; Genty et al., 2001, 2003).

5.2.2. Sr/Ca as proxy for infiltration dynamics

Speleothem Sr/Ca constitutes a sensitive proxy for infiltration changes in the epikarst, with higher values being recorded during times of reduced effective moisture availability (Fairchild and Treble, 2009). Other mechanisms can explain Sr mobility within the epikarst and include changes in weathering rates, aerosol input, soil activity (Verheyden et al., 2000; Fairchild et al., 2006; Baker et al., 2021; Sinclair et al., 2012) that can induce high-frequency variability on short timescales (decadal to annual). At the Cueva Chica, speleothem Sr/Ca reacts to local infiltration changes and climate saisonnality with i) high precipitation and effective infiltration in austral winter and, ii) low precipitation and high potential evapotranspiration during austral summer (Fig. 1B). Long-term drier climate with shorter wet seasons and low precipitation can lead to open conditions in soil and epikarst, and strong CO_2 degassing from infiltrating water and in the cave atmosphere. These processes can lead to PCP within the epikarst (Verheyden et al., 2000; Fairchild et al.,

2006), which in turn leads to higher Sr concentration in the aqueous solution and ultimately in the speleothem (Verheyden et al., 2000; Fairchild and Treble, 2009).

5.2.3. Speleothem and dripwater $\delta^{18}O$

Calcite $\delta^{18}O$ is generally interpreted as related to precipitation amount, atmospheric circulation pattern, seasonal changes in infiltration (McDermott, 2004; Dreybrodt and Scholtz, 2011). Additionally, local factors can affect $\delta^{18}O$ in the epikarst and cave, including evaporation and CO_2 degassing, temperature, and mixing of older and younger water in the epikarst (Mühlinghaus et al., 2009). Chica cave receives precipitation mainly from the Pacific Ocean through WSW winds. These waters are characterized by low $\delta^{18}O$ in precipitation ($\delta^{18}O_p$) values (Suppl. S4) and fall on the GMWL, while water collected during spring and summer show high $\delta^{18}O_p$. Effective infiltration and epikarst recharge are biased towards the winter season and possibly early summer. Dripwater collected in Chica and nearby Milodon caves in early summer show $\delta^{18}O_{drip}$ values biased towards autumn-winter $\delta^{18}O_p$. Unfortunately, no dripwater is available from other seasons.

Even though the sampling site is deep inside the cave (60 m from the entrance) with high relative humidity, we cannot strictly exclude the possibility that evaporation affected dripwater $\delta^{18}O$. Cave ventilation could lower relative humidity sufficiently to induce evaporation. The temperature effect on $\delta^{18}O_{drip}$ is unlikely a major factor because cave air temperature does not vary significantly ($T_{cave\ air} = 4.6 \pm 0.6$°C).

Finally, mixing of infiltration waters of different age in the epikarst likely results in the observed relatively stable $\delta^{18}O_{drip}$ values through a year (Suppl. fig. 6, table 2). The small offset between the two S6 and S8 speleothems suggests some degree of mixing along the individual water pathways to the two sampling sites. The water residence time in the epikarst is likely on the order of months to years. The epikarst thickness above Chica cave (40 m) is similar to that observed at Ernesto (Italy), Han sur Lesse (Belgium) or Bunker (Germany) caves (epikarst thickness between 15 and 30 m, Van Rampelbergh et al., 2014; Kluge et al., 2010; Miorandi et al., 2010) where lags of several months to years between surface and cave are found. Given the observed narrow range of $\delta^{18}O$ in dripwaters (Fig. 4) and infiltration pattern (Suppl., fig. 6) we suggest that both dripwater and speleothem $\delta^{18}O$ values represent a buffered (multi-)annual mean signal, likely biased towards the winter season.

The Chica $\delta^{18}O_{cc}$ record (Fig. 3A) thus integrates a complex signal of precipitation history and corresponding $\delta^{18}O_p$. Earlier work on three speleothems combined with intensive cave microclimate monitoring in Marcello Arévalo (53°S), an open-air cave located further south, showed that $\delta^{13}C$ and $\delta^{18}O$ were both linked to effective infiltration (Schimpf et al., 2011). There, the most suitable stalagmites preserving the link between stable isotope signal and effective infiltration in MA cave were the ones showing high and constant growth rates (>67 µm/a). In our case, the flowstone S6-S6bis in the Chica cave grew mostly continuously, with limited growth from 5 to 3 ka BP, and growth rates suggest that S6 was regularly submerged. A high growth rate of 132 µm/a is found prior to 9 ka that subsequently slowed to *ca*. 33 µm/a over the course of the Holocene until recent time. Stalagmite S8 grew relatively fast at a rate of 111 µm/a from 6 to 5 ka BP, and slowly at a rate of 11 µm/a after 4 ka BP. We suggest then that variations in the Chica $\delta^{18}O$ signal reflect mainly changes in amount of precipitation and effective infiltration, and to some extent changing moisture transport trajectories throughout the Holocene.

5.3. General climatic conditions during the Holocene in southwest Patagonia

The combined stable isotope, growth rate, and Sr/Ca time series suggest three climatic regimes throughout the last 12 ka in Southern Patagonia: i) an early Holocene wet period (with the exception of two dry excursions at 10.5 ka and 8.5 ka BP), ii) a mid-Holocene dry period and iii), a return to generally wet conditions over the late Holocene.

5.3.1. The early Holocene humid period (12-8.5 ka BP)

During the early Holocene period, the $\delta^{18}O_{cc}$ values are low until 8.5 ka BP, except for two excursions at 10.5 ka and 8.5 ka BP (Fig. 6). The $\delta^{18}O$ values are the lowest of the entire Holocene record and vary between -7 and -9 ‰, suggesting relatively wet conditions. This notion is supported by a high growth rate of ca. 60-170 µm/year. The flowstone grew continuously under sufficiently humid conditions to maintain infiltration in the epikarst zone and limited PCP as indicated by low Sr/Ca and low but highly variable $\delta^{13}C$ values (Fig. 3A). The study site was likely covered by broad-leaved mixed C3/C4 type vegetation on a developed soil

with higher CO_2 production through biogenic activity. The onset of this wet early Holocene period agrees closely with abundant *N. dombeyi* pollen in the Vega Benitez peat profile (McCulloch et al., 2021), suggesting a developed woodland cover. A similarly developed *Nothofagus* forest was found in the Punta Burslem pollen records (McCulloch et al., 2020) further South. Other records from lake Tamar and peat GC2 also suggest a wet period with a peak in humidity around 11 ka BP (Fig. 5A) (Lamy et al., 2010). Both, high abundance of hygrophytic taxa (a sensitive proxy for extremely humid environments) at peat GC2, and high terrestrial organic carbon concentrations linked to extreme rainfall events at lake Tamar (Lamy et al., 2010) are indicative of humid conditions.

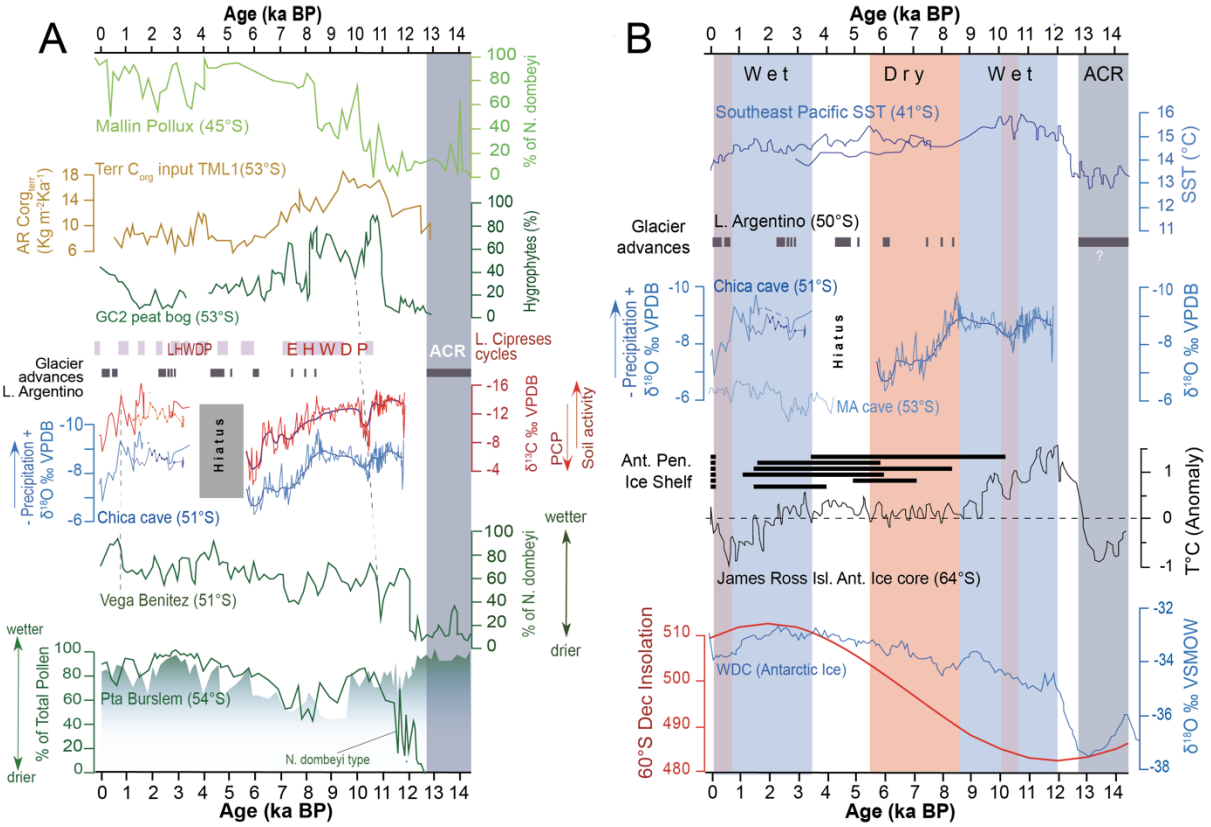

Fig. 6*. The $\delta^{18}O$ and $\delta^{13}C$ records of Cueva Chica compared with global and regional records for the last 14 ka.* ***A.*** *(top to base) Comparison of continental records in Southern Chile, including the % Nothofagus dombeyi pollen from Mallin Pollux (Markgraf et al., 2007), terrestrial organic carbon in lake Tamar (Lamy et al., 2010), % hygrophytes from peat bog GC2 (Lamy et al., 2010), lago Cipreses warm cycles (Moreno et al., 2018), moraine building events in the Lago Argentino basin (Kaplan et al., 2016) & glacial fluctuations in the Marinelli fjord (Hall et al., 2019), Cueva Chica isotope record (this study), % of Nothofagus dombeyi pollen from Vega Benitez (McCulloch et al., 2021) and % of Nothofagus dombeyi pollen vs total normal pollen from Punta Burslem (McCulloch et al., 2020). ACR timing is indicated by blue shade from Gest et al. (2017).* ***B.*** *(top to base) Comparison of global and regional records in Southern Chile, including sea surface temperatures (SSTs) from GeoB3313-1 (Lamy et al., 2002) and ODP1233 (Lamy et al., 2015), moraine building events from Lago Argentino (Kaplan et al., 2016), Cueva Chica $\delta^{18}O$, Marcello Arévalo (MA) speleothem $\delta^{18}O$ (Schimpf et al., 2011), periods of open marine conditions in Prince Gustav Channel, Antarctic Peninsula & T anomalies from James Ross Island (Mulvaney et al., 2012), $\delta^{18}O$ from West Dome C (WDPM, 2013) and 60°S december insolation (Berger & Loutre, 1991). Red rectangles indicate dry periods and blue rectangles wet periods defined by the Cueva Chica speleothem record.*

The early Holocene dry episode begins with a positive excursion of $\delta^{18}O$ and $\delta^{13}C$ centred at 10.5 ka BP, concurrent with high Sr/Ca values. Between 10.7 ka and 10.2 ka BP (Fig. 6A), the Cueva Chica isotopic profile records significant drying with a short-lived low rainfall period impacting the vegetation cover on the Cerro Benitez. At the Vega Benitez site upstream of the Chica cave watershed, *N. dombeyi* forest declined from 11.54–10.78 cal ka BP and was replaced by *Poaceae* and *Cyperaceae* taxa. This shift in pollen assemblages is typical of a continued transition from lake to a peat bog and the increase in *Poaceae* and *Cyperaceae* likely reflects the spread of grasses and sedges over the emerging bog surface (McCulloch et al., 2021). This reduction of water surface suggests less water availability and overall reduced local precipitation, which supports the dry event recorded in the Chica record. The different timing of the dry event in the Chica samples (10.7-10.2 ka BP) and in nearby lake Vega Benitez (11.5–10.7 ka BP) is likely

related to limited chronological control in both archives. It is worth mentioning that comparable drying events are found in other regional records between 11 and 10 ka BP, including a rapid decline in *N. dombeyi* in the Punta Burslem peat bog (McCulloch et al., 2020) and a clear reduction in the abundance of hygrophytes in the GC2 peat bog (Lamy et al., 2010). After 10.2 ka BP, increased moisture availability is noticeable in the $\delta^{18}O$ profile with the most negative values of the whole record centred at 8.5 ka BP (Fig. 6A). The $\delta^{13}C$ values start to become more negative, but not below -12 ‰. This wet phase is less prominent than the early Holocene period, but still noticeable in the Vega Benitez pollen record, with short-lived peaks in *N.dombeyi* pollen at 10.7 and 8.2 ka BP (McCulloch et al., 2021).

5.3.2. The mid-Holocene drying trend (8.5- 5.8 ka)

After 8 ka BP, a slow trend towards higher $\delta^{13}C$ values in the Chica record is mirrored in a persistent rise in the number of deteriorated pollen and a corresponding decrease of well preserved pollen in most of the remaining record of Vega Benitez (McCulloch et al., 2021). Overall, the changing $\delta^{13}C$ trend and pollen assemblages as well as differential pollen preservation indicate reduced moisture availability. The trend in the $\delta^{13}C$ profile and a corresponding two permil shift to higher $\delta^{18}O$ shows the onset of a robust change in vegetation cover induced by reduced precipitation and less effective infiltration until 5.8 ka BP. The clear trend in the Chica record confirms regional drying as interpreted from reduced hygrophytic taxa in the GC2 peat bog and lower terrestrial organic carbon concentrations in lake Tamar. Further South, low abundance of *N. dombeyi* between 10 ka and 7 ka BP in Punta Burslem (McCulloch et al., 2020) also suggests drier conditions. The response of all the records indicates a consistent drying trend across 50°S to 55.5°S. This trend seems to be contrasted by the Mallin Pollux pollen profile further North (Markgraf et al., 2007), which might mark a contrasting N-S climatic gradient, although additional records would be required to confirm this interpretation.

5.3.3. Return to wet conditions during late Holocene (4-0.5 ka BP)

From 4 to 0.7 ka BP, decreasing $\delta^{18}O$ and $\delta^{13}C$ values in the Chica record reflect a return of more humid conditions. This coincides with a relatively humid phase in the Vega Benitez (McCulloch et al., 2021) where four successive peaks in *N.dombeyi* abundance are observed at 3.3, 2.8, 2, and 0.7 ka BP (Fig. 6A). Low $\delta^{18}O$ in Marcello Arévalo (MA) speleothem (53°S) indicates wet conditions from 2.5 to 0.7 ka BP. Higher *N. dombeyi* concentrations in Burslem peat record confirm this interpretation, but no clear humid phase is found in Lake Tamar during the late Holocene. After 0.7 ka BP, our stable isotope record increases again and suggests the return of drier local conditions. This agrees with reduced *N.dombeyi* abundance in the Vega Benitez record and a similar trend in the MA stable isotope records.

5.4. Global and regional drivers of climate variability in SW Patagonia

The flowstone in the Chica cave started to grow significantly from 12 ka onwards during a period of high Pacific SST (Lamy et al., 2002; 2015), with > 4°C warming after the Antarctic Cold reversal (ACR) (Fig. 6B). A similar temperature shift is observed at the same time in the Antarctic James Ross Island ice core, and a trend towards higher $\delta^{18}O$ is found in Antarctic ice from West Dome C (Weiss divide project members, 2013). Both observations mark the onset of deglaciation in Antarctica and a reduction in sea-ice cover. Despite minimum summer insolation at 11-12 ka BP in the Southern hemisphere (Berger and Loutre, 1991), the early Holocene was the warmest period in Southernmost South America, consistent with ice core data and the rise in SST in the South Pacific. This warming in both polar ice and Southern Ocean surface coincides with enhancement of the southwesterly winds (SWW) in the centre of the wind belt (Lamy et al., 2010), but is difficult to explain by orbital forcing. The warming during the early Holocene might be attributable to changes in global ocean circulation which involves a bipolar seesaw-like surface temperature pattern (Lamy et al., 2010) and a rise in air temperature in the southern hemisphere (Ganopolski et al., 1998; Hodell et al., 2001). A response of the SWW to changes in the strength of the Atlantic meridional overturning circulation (AMOC) has been previously proposed for Termination 1 (Lamy et al., 2007). Model experiments (Timmermann et al., 2005) suggest a rapid signal transfer between the AMOC and SSW shifts with an increase of SWW strength south of 50°S and decreased wind strength in the mid-latitudes between 40° to 50°S. The response of terrestrial archives in Southern Patagonia to this atmosphere/ocean feedback is reflected in a reduction of glacier advances in Lago Argentino (50°S) and higher precipitation at Cerro Benitez (Cueva Chica) and the Chilean coast, likely in concert with higer temperatures.

From 9 to 5 ka BP, a slight decrease in SE Pacific SST went hand in hand with a minor temperature decrease in on James Ross Island (64°S) (Fig. 6B). The most significant change in regional conditions was increased

ice-shelf instability along the Antarctic Peninsula (Mulvaney et al., 2012), that began around 10 ka BP and expanded gradually after 9 ka BP. The intensification of ice-shelf instability along the Antarctic Peninsula is concordant with increasing summer insolation in the Southern hemisphere, which intensified a poleward shift of the SWWs in response to global warming (McCulloch et al., 2020). Over the Patagonian landmass, this implied a reduction in moisture supply from the Pacific onto the Patagonian shore, lower total precipitation over the Chica cave and decreased glacier advances (warm/dry conditions) at Lago Argentina (50°S). After 5 ka BP, a different climatic background arises in Southern Patagonia, with SST and the James Ross Island ice core records indicating a gradual temperature decline (Fig. 6B). This pattern is consistent with an equatorward shift of the SWWs in response to a cooling Southern hemisphere, known as the Neoglacial period. Despite increasing insolation in the Southern hemisphere the Neoglacial cooling began at least *ca.* 5 ka BP (Glasser et al., 2004). In turn, increased AMOC exported heat from the South Atlantic to the North Atlantic, triggering sea-ice growth around Antarctica and glacial advances in Southern Patagonia such as at Lago Argentino (Fig. 6B). One global feedback at the end of the mid-Holocene is the establishment of modern El Niño-Southern Oscillation (ENSO) frequencies (Clement et al., 1999; Moy et al., 2002). The SWW storm tracks extended to lower latitudes, inducing a return to wetter conditions along the Patagonian coast, as found in both Marcello Arévalo speleothem and Chica records after 4 ka BP. However, moisture patterns were highly variable due to increased insolation seasonality (Markgraf et al., 2000) and intensified ENSO (Moreno, 2004). This increased variability with rapid climate change (RCC) is recorded in several lake records (Fletcher and Moreno, 2011; Moreno, 2004; 2018b), but less clear in Cueva Chica speleothems, although the $\delta^{18}O$ signal seems to be more variable.

5.5. Interpretation of fluid inclusion δD and $\delta^{18}O$

Speleothems fluid inclusions (FI) can retain the original isotopic composition on 'fossil' dripwater (Affolter et al., 2014 ; Matthews et al., 2021, van Breukelen et al, 2008; Wassenburg et al., 2021 ; Warken et al. 2022). When fluid inclusions are well-preserved, FI isotope data ($\delta^{18}O$; δD) fall onto or near the modern LMWL while a significantly lower regression slope of FI isotope results would indicate secondary evaporation (Clark and Fritz, 1999). If the FI_{water} indeed mirrors the original precipitation, the slope would reflect humidity during and after precipitation. Slope values decrease with humidity (e.g., a slope of 4.5 would indicate humidity levels of 50%). Fluid inclusion samples from the Chica S6 core reveal some intriguing complexity. While some samples fall near the LMWL, more than 50% of the samples diverge with a slope of 1.4 (Fig. 4). This line resembles a secondary evaporation line, which could result from cave ventilation (Nehme et al. 2020; Warken et al. 2022), but the slope of the line is unusually low for such evaporation scenario (Clark and Fritz, 1999), which suggests that other processes must be at work, like diagenetic alteration of fluid inclusion water (Uemura, 2020), or an analytical artefact leading to incomplete water extraction from the fluid inclusions. (Suppl. S5 table 3, comments).

The line of reasoning described here reduces essentially the most trustworthy FI data to samples with the lowest isotope values in Fig. 4 and closest to LMWL. The trustworthy FI isotope dataset can be therefore reduced to a single projected dripwater value ($\delta^{18}O$: -11.8‰ ; δD : -87‰) for the time interval (8.5 to 11.3 ka BP) covered in the data. Since almost all fluid inclusion samples represent a short time interval in the earliest Holocene, the projected isotope values should be representative of the beginning of the Holocene. Considering the uncertainties in our projections, we believe values given from FI-3, FI-5 and FI-8b samples (Suppl., table 3) are not significantly different from the modern-day dripwater values (Fig. 4).

5.6. Temperature estimates based on FI and D47

Clumped isotope temperatures ($T\Delta_{47}$) offer the prospect to reconstruct the temperature at which the speleothem formed, independent of the isotopic composition of the dripwater. Previous work (Daeron et al. 2019; Fiebig et al., 2021) suggests that cave carbonates precipitated near isotopic equilibrium conditions retain their original $T\Delta_{47}$ signal. Unfortunately, kinetic isotope fractionation, induced by rapid CO_2-degassing or evaporation of dripwater can overprint the original clumped isotope signal and render derived temperatures unrealistic. This kinetic effect on speleothem is well known and has been studied previously (Affek et al., 2014; Kluge et al., 2013; Guo and Zhou, 2019, Matthews et al., 2021). Kinetic effects caused can be evaluated by comparing FI stable isotopes and dripwater isotope data (Fig. 4). Samples close to the LMWL can be regarded as trustworthy, whereas samples located well below the modern LMWL are likely to be affected by secondary evaporation. This means that FI-based temperature estimates from samples with $\delta^{18}O$ values <-8 permil (Fig. 4) might reflect environmental temperatures, while temperature estimates from samples with higher $\delta^{18}O$ values should be discarded.

Our samples display $T\Delta_{47}$ values between 4.8±1.3°C and 17.4±1.6°C, higher than modern cave air temperature (5±1°C) (Fig. 7). Four samples (C1, C2, C5b, C6) overlap within error with modern cave air temperature, but the remaining four (C0, C3, C4, C5) are significantly higher than expected (Fig. 7). Sample C1 is taken from inside a soda straw that was embedded in the floor after breakage. It is likely that the soda straw remained filled with water as long as it was actively dripping, therefore constantly replenishing the DIC pool. At the same time, CO_2-degassing was likely limited by the barrier of the soda straw walls and a thick water column inside (Smith, 2021). These conditions support the recording of unaltered clumped isotope signals and we trust the observed $T\Delta_{47}$ value. Sedimentological evidence suggests that sample C2 precipitated as cave pool carbonate under subaqueous conditions that limit rapid CO_2-degassing. Under such conditions the clumped isotope signature is likely to remain unaltered by kinetic fractionation (Kele et al 2015, Breitenbach et al. 2018, Drysdale et al. 2020). These two samples suggest that, starting from at least 2.5 ka, mean temperatures in the Cerro Benitez were close to modern (Fig. 7).

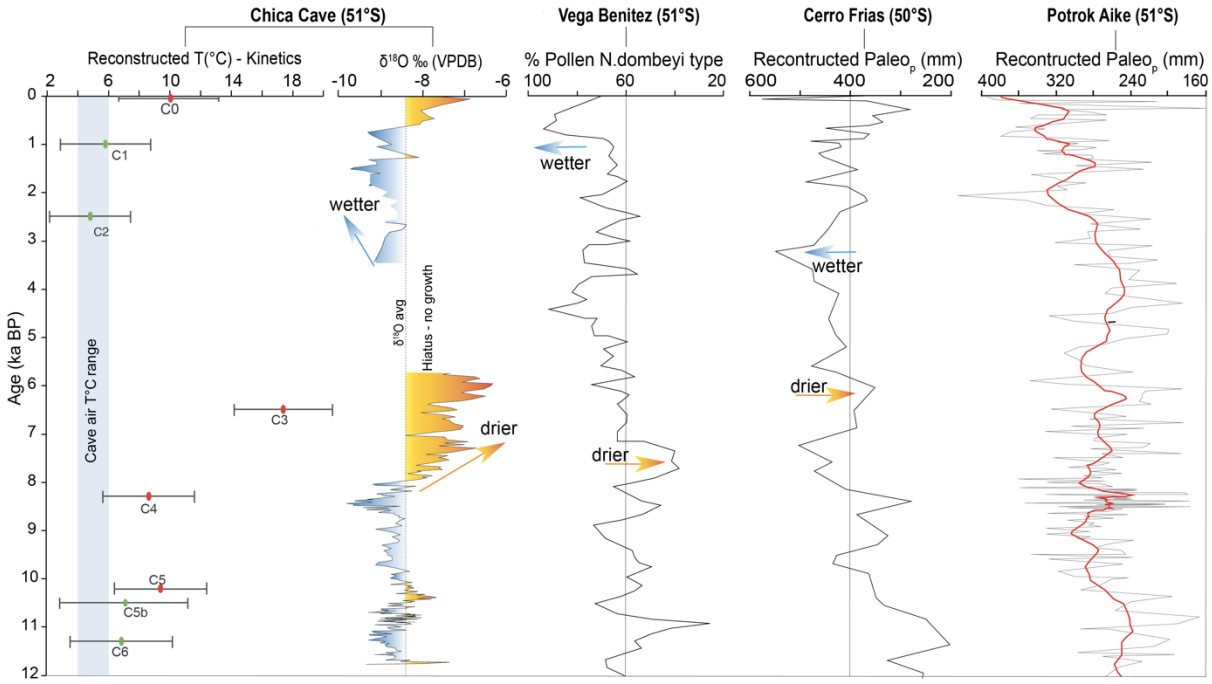

***Fig.** 7. The T-Kinetics distribution of the measured clumped isotopes (x axis) and the modern cave air are reported within 2s error. The values indicated in green are samples with less kinetics and close to the modern cave air, the ones in red are samples with high kinetics and shifted towards higher temperatures. For comparison, are the Chica cave' $\delta^{18}O$ signal and the pollen % from the Vega Benitez peat (McCulloch et al., 2021) as indicator of dryness/wetness trend in the Cerro Benitez. For regional comparison, the reconstructed paleoprecipitation from pollen record of the Cerro Frias peat (Tonello et al., 2009) to the North and from pollen record of Potrok Aike Lake in the Argentinian pampa (Shabitz et al., 2013) to the East.*

Similarly, samples C5b and C6 from the early Holocene were likely deposited from a thicker water film under wetter conditions and their clumped isotope temperatures are likely valid. While their $T\Delta_{47}$ values overlap with the modern temperature, the large error margins do not allow us to establish whether the early Holocene was significantly warmer than today or not. If minimal kinetic fractionation is expected, $T\Delta_{47}$ (max 10°C) might well align with globally higher-than-modern temperatures (6±3°C) between 10.8 and 10.3 ka. The samples C0, C4 and C5 show temperatures only slightly higher than today and might be realistic, although we cannot exclude any impact of kinetic fractionation and thus 'to high" reconstructed temperatures. The remaining sample C3 is unrealistically high and kinetic fractionation due to CO_2-degassing and/or evaporation is sucpected to affect this sample. A trend towards less negative $\delta^{18}O$ values shortly after that sample is noticeable, which might be interpreted as local drying that lead to an increased kinetic fractionation.

To summarize, local temperatures might have been slighly higher in the early Holocene (11-8 ka BP) compared to today (Fig. 7), although the large error margins do not allow a quantitative estimation of such warming. Local temperatures were similar to today since at least 2.6 ka BP. A dry interval around 8.5 - 5.5 ka likely affected the cave's hydrology such that kinetic fractionation altered the clumped isotope system, resulting in too warm apparent reconstructed temperature. The comparison of local reconstructed T(°C) from Chica cave with other semi-quantitative (Pollen) signals from Vega Benitez marsh and reconstructucted

paleo-precipitation from Cerro Frias (Fig. 7), show a regional similarity in the drying trend during time interval 8.5 - 5.5 ka and a return to wet conditions from 3.5 to 1 ka. However, the climatic paleo-precipitation trend shown from Potrok Aiketo the East seems to be out of phase with the Andean records.

6. Conclusions

The Cueva Chica record from the Cerro Benitez (51°S) in one of the rare studied carbonate record located far South in the Southern Andes. This study provides a first highly-resolved isotopic, elemental and paleotemperature record spanning the Holocene from the last 12 ka, albeit with a hiatus from 5.8 to 4 ka BP. The stable isotope and trace elements curves from speleothems show a covariability in the signals. First, cave monitoring and comparision with regional climatic data suggest that both dripwater and speleothem $\delta^{18}O$ values represent a buffered (multi-)annual mean signal, likely biased towards the winter season. Overall, the oxygen isotope signal reflects changes in amount of precipitation and effective infiltration in the studied site, and to some extent changing moisture transport trajectories throughout the Holocene. Second, $\delta^{13}C$ signal reflects a combined signal of epikarst and in-cave CO_2 degassing, vegetation composition and density as well as soil activity. Third, the Sr/Ca elemental data shows a moderate sensitiveness to infiltration changes in the epikarst and behave in concert with the $\delta^{13}C$ signal, albeit with different intensitiy to dryness between both proxies.

The multi-proxy analysis of the petrography, growth rate, stable isotopes and elemental data in the Chica record suggest three main climatic phases throughout the last 12 ka in Southern Patagonia: i) an early Holocene wet period (with the exception of two dry excursions at 10.5 ka and 8.5 ka BP), ii) a mid-Holocene dry period and iii), a return to generally wet conditions over the late Holocene. The climate variability from the Chica record is in phase with other regional peat and lake records located between 50° ant 55°S along the Andes mountain corridor and Western Pacific side, but is out of phase with records located North to 50° latitude.

These tri-phased climate regimes recorded in the Chica cave are the result of global drivers controlling the strength and shifts of the SWWs throughout the Holocene. The early Holcene was the warmest period in Southernmost South America, and might be attributable to changes in global ocean circulation which involves a rise in air temperature and a strength in SWW from 50°S. The response over landmass in Southern Patagonia is higher precipitation over the Chica cave and the Chilean coast, likely in concert with higer temperatures. After 9 ka BP, an intensification of ice-shelf instability along the Antarctic Peninsula is concordant with increasing summer insolation in the Southern hemisphere, which intensified a poleward shift of the SWWs in response to global warming. This significant change in regional conditions implied a reduction in moisture supply from the Pacific onto the Patagonian shore and lower total precipitation over the Chica cave. After 5 ka BP, a different climatic background arises, with a gradual SST decline, consistent with an equatorward shift of the SWWs in response to a cooling Southern hemisphere, known as the Neoglacial period. The SWW storm tracks extended to lower latitudes, inducing a return to wetter conditions with highly variable moisture patterns along the Patagonian coast, as found in the Cueva Chica and other terrestrial records after 4 ka BP.

The reconstructed paleotemperatures based on fluid inclusisons and ($T\Delta_{47}$) from the Cueva Chica speleothems provide a reasonable estimation of past terrestrial temperature in the Cerro Benitez throughout the Holocene: local temperatures might have been slighly higher in the early Holocene (11-8 ka BP BP) compared to today. A dry interval around 8.5 - 5.5 ka BP likely affected the cave's hydrology such that kinetic fractionation altered the clumped isotope system, resulting in too warm apparent reconstructed temperature. Since at least 2.6 ka BP, local temperatures were similar to today.

7. Acknowledgments.

We thank the Corporación Nacional Forestal Chile (CONAF) authorities and the rangers of the Park "Monumento Natural Cueva del Milodón" for their permission to sample in the Cueva Chica. Jorge Canales Helmer and Mario Margoni are thanked for the permission they gave to work in their properties. Both Proyecto Fondo Nacional de Desarrollo Científico y Tecnológico (**FONDECYT** ; PI: F.Martin**) funding project n°1180272** and the Centre National pour la Recherche Scientifique (**CNRS**) funding project **PICS-GEOCEBE** ; PI: D.Todisco): Geoarchaeology of caves from Cerro Benitez, Última Esperanza, Chilean Patagonia (2017-2019) supported field investigations, sample shipment and laboratory analysis.

8. CRediT author statement

C. Nehme: conceptualization, writing-original draft preparation, field investigation and sampling, analysis; **D. Todisco** : conceptualization, field investigation and sampling, reviewing & editing, funding acquisition ; **S. Breitenbach** : analysis, software validation, writing, review & editing ; **I. Couchoud** : conceptualization, analysis, writing, review & editing ; **M. Marchegiano** : analysis, validation, writing; **M. Peral** : analysis, validation, writing ; **H. Vonhof** : analysis, validation, writing ; J. Hellstrom : analysis, **R. Tjallingi** : analysis, writing ; **Ph. Claeys** : supervision ; **L. Borrero** : review & editing ; **F. Martin** : field investigation, review & editing, funding acquisition and head of the project.

9. competing interests statement

The authors have no conflict of interests to declare.

10. References

Aceituno P., Fuenzalida H., Rosenbluth B. 1993. Climate along the extratropical West Coast of South American'. In Mooney, H.A., Fuentes, E.R., Kronberg, B.I. (eds), Earth System Responses to Global Change, Academic Press, New York, p. 365.

Affek H.P., Bar-Matthews M., Ayalon A., Matthews A., Eiler J.M., 2008. Glacial/interglacial temperature variations in Soreq cave speleothems as recorded by 'clumped isotope' thermometry. *Geochim. Cosmochim. Acta, 72*(22), 5351-5360

Affek H.P., Zaarur S., 2014. Kinetic isotope effect in CO_2 degassing: Insight from clumped and oxygen isotopes in laboratory precipitation experiments. *Geochim. Cosmochim. Acta*, *143*, 319-330.

Affolter S., Fleitmann D., Leuenberger M., 2014. New online method for water isotope analysis of speleothem fluid inclusions using laser absorption spectroscopy (WS-CRDS). *Clim. Past*, *10*(4), 1291-1304.

Alloway B.V., Pearce N.J., Moreno P.I., Villarosa G., Jara I., De Pol-Holz R., Outes V., 2017. An 18,000 year-long eruptive record from Volcán Chaitén, northwestern Patagonia: Paleoenvironmental and hazard-assessment implications. *Quat. Sci. Rev*, 168, 151-181.

Anderson N.T., Kelson J.R., Kele S., Daëron M., Bonifacie M., Horita J., Mackey T.J., John C.M., Kluge T., Petschnig P., Jost A.B., Huntington K.W., Bernasconi S.M., Bergmann K.D., 2021. A Unified Clumped Isotope Thermometer Calibration (0.5–1,100°C) Using Carbonate-Based Standardization, *Geophys. Res. Lett.,* 48, e2020GL092069.

Baker, A., Mariethoz, G., Comas-Bru, L., Hartmann, A., Frisia, S., Borsato, A., ... & Asrat, A. (2021). The Properties of Annually Laminated Stalagmites-A Global Synthesis. *Reviews of Geophysics*, *59*(2), e2020RG000722.

Bakun A., Field D.B., Redondo-Rodriguez A.N.A., Weeks S.J., 2010. Greenhouse gas, upwelling-favorable winds, and the future of coastal ocean upwelling ecosystems. *Global Change Biology*, 16(4), 1213-1228.

Baldini J.U.L., Lechleitner A.F., Breitenbach S.F.M., van Hunen J., Baldini L. M., Wynn P.M., Jamieson R.A., Ridley H.A., Baker A.J., Walczak I.W. Fohlmeister J., 2021. Detecting & quantifying palaeoseasonality in stalagmites using geochemical and modelling approaches. *Quat. Sci. Rev.,* 106784.

Berger A., Loutre M.F., 1991. Insolation values for the climate of the last 10 million years. *Quat. Sci. Rev., 10*(4), 297-317.

Bernasconi S.M., Daëron M., Bergmann K.D., Bonifacie M., Meckler A.N., Affek H.P. ,…& Ziegler M., 2021. InterCarb: A community effort to improve interlaboratory standardization of the carbonate clumped isotope thermometer using carbonate standards. *Geochem., Geophys.*, *22*(5), e2020GC009588.

Borrero L.A., Franco N.V., 1997. Early Patagonian hunter-gatherers: subsistence and technology. *J. of Anthropol. Res.*, *53*(2), 219-239.

Brand W.A., Assonov S.S., Coplen T.B., 2010. Correction for the ^{17}O interference in $\delta^{13}C$ measurements when analyzing CO_2 with stable isotope mass spectrometry (IUPAC Technical Report), *Pure & Applied Chemistry*, 82, 1719-1733.

Breitenbach S.F.M., Rehfeld K., Goswami B., Baldini J.U.L., Ridley H.E., Kennett D.J., Prufer K.M., et al., 2012. Constructing proxy records from age models (COPRA). *Clim. Past*, 8, 1765-1779.

Breitenbach S.F., Mleneck-Vautravers M.J., Grauel A.L., Lo L., Bernasconi S.M., Müller I.A.,... & Hodell D.A., 2018. Coupled Mg/Ca and clumped isotope analyses of foraminifera provide consistent water temperatures. *Geochim. Cosmochim. Acta,* , *236*, 283-296.

Bronk Ramsey C.B., 2009. Bayesian analysis of radiocarbon dates. *Radiocarbon*, *51*(1), 337-360.

Cerling T.E. and Quade J., 1993. Climate change in continental isotopic records. *Geophys. Monograph*, *78*, 217-231.

Cheng H., Zhang P.Z., Spötl C., Edwards R.L., Cai Y.J., Zhang D.Z., Sang W.C., Tan M., An Z.S., 2012. The climatic cyclicity in semiarid-arid central Asia over the past 500,000 years. *Geophys. Res. Lett.*, *39*(1).

Clark I., Fritz P., 1999. Water-Rock Interaction, in: Environmental Isotopes in Hydrogeology, Lewis Publishers, New York, 245–266,.

Clement A.C., Seager R., Cane M.A., 1999. Orbital controls on the El Nino/Southern Oscillation and the tropical climate. *Paleoceanography*, *14*(4), 441-456.

Daëron M., 2021. Full Propagation of Analytical Uncertainties in Δ^{47} Measurements, *Geochem. Geophys. Geosyst*., 22, e2020GC009592

Daëron M., Blamart D., Peral M., Affek H.P., 2016. Absolute isotopic abundance ratios and the accuracy of Δ^{47} measurements, *Chem. Geol.*, 442, 83-96.

Daëron M., Drysdale R.N., Peral M., Huyghe D., Blamart D., Coplen T.B., ... & Zanchetta G., 2019. Most Earth-surface calcites precipitate out of isotopic equilibrium. *Nature communications*, *10*(1), 1-7.

De Graaf S., Lüders V., Banks D.A., Sośnicka M., Reijmer J.J., Kaden H., Vonhof H.B., 2020. Fluid evolution & ore deposition in the Harz Mountains revisited: isotope & crush-leach analyses of fluid inclusions. *Mineralium Deposita*, *55*(1), 47-62.

Deininger M., Fohlmeister J., Scholz D., Mangini A., 2012. Isotope disequilibrium effects: The influence of evaporation and ventilation effects on the carbon and oxygen isotope composition of speleothems–A model approach. *Geochim. Cosmochim. Acta*, *96*, 57-79.

De Vleeschouwer D., Peral M., Marchegiano M., Füllberg A., Goderis S., Meinicke N., Petrick B., Snoeck C., Pälike H., Claeys P., 2021. Plio-Pleistocene Perth Basin water temperatures and oxygen and clumped isotope paleothermometry. *Clim. Past Discussions*, 10.5194/cp-2021-151

Dirección Meteorológica de Chile, 2019. www.meteochile.gob.cl/inicio.php

Dreybrodt W., Scholz D., 2011. Climatic dependence of stable carbon and oxygen isotope signais recorded in speleothems: From soil water to speleothem calcite, *Geochim. Cosmochim. Acta*, 75, 734-7 52.

Drysdale R.N., Paul B.T., Hellstrom J.C., Couchoud I., Greig A., Bajo P., Woodhead J.D., 2012. Precise microsampling of poorly laminated speleothems for U-series dating. *Quat. Geochronol.*, *14*, 38-47.

Drysdale R., Couchoud I., Zanchetta G., Isola I., Regattieri E., Hellstrom J., .. & Woodhead J., 2020. Magnesium in subaqueous speleothems as a potential palaeotemperature proxy. *Nature communications*, *11*(1), 1-11.

Eiler J.M., 2007. Clumped-isotope geochemistry -The study of naturally-occurring, multiply-substituted isotopologues. *Earth Planet. Sci. Lett.*, , 262(3-4), 309-327.

Eiler J.M., 2011. Paleoclimate reconstruction using carbonate clumped isotope thermometry. *Quat. Sci. Rev* 30(25-26), 3575-3588.

Fairchild I.J., Baker A. *Speleothem science: from process to past environments*. Vol. 3. John Wiley & Sons, 2012.

Fairchild I.J., Treble P.C., 2009. Trace elements in speleothems as recorders of environmental change. *Quat. Sci. Rev*, *28*(5-6), 449-468.

Fairchild I.J., Smith C.L., Baker A., Fuller L., Spötl C., Mattey D., McDermott F., 2006. Modification and preservation of environmental signals in speleothems. *Earth Sci. Rev.*, *75*(1-4), 105-153.

Fiebig J., Daëron M., Bernecker M., Guo W., Schneider G., Boch R., ... & Dietzel M., 2021. Calibration of the dual clumped isotope thermometer for carbonates. *Geochim. Cosmochim. Acta*, 312, 235-256.

Fletcher M.S., Moreno P.I., 2011. Zonally symmetric changes in the strength and position of the Southern Westerlies drove atmospheric CO^2 variations over the past 14 ky. *Geology*, *39*(5), 419-422.

Fohlmeister J., Scholz D., Kromer B., Mangini A., 2011. Modelling carbon isotopes of carbonates in cave drip water. *Geochim. Cosmochim. Acta*, *75*(18), 5219-5228.

Ganopolski A., Kubatzki C., Claussen M., Brovkin V., Petoukhov V., 1998. The influence of vegetation-atmosphere-ocean interaction on climate during the mid-Holocene. *Science*, *280*(5371), 1916-1919.

Garreaud R., Lopez P., Minvielle M., Rojas M., 2013. Large-scale control on the Patagonian climate. *J. Clim.*, *26*(1), 215-230.

Genty D., Baker A., Massault M., Proctor C., Gilmour M., Pons-Branchu E., Hamelin B., 2001. Dead carbon in stalagmites: carbonate bedrock paleodissolution vs. ageing of soil organic matter. Implications for ^{13}C variations in speleothems. *Geochim. Cosmochim. Acta, 65*(20), 3443-3457.

Genty D., Blamart D., Ouahdi R., Gilmour M., Baker A., Jouzel J., Van-Exter S., 2003. Precise dating of Dansgaard–Oeschger climate oscillations in western Europe from stalagmite data. *Nature*, *421*(6925), 833-837.

Girault I., Todisco D., Çiner A., Sarıkaya M.A., Yıldırım C., Quiquerez A., Martin F., Borrero L., Fabel D., Grandjean P., Nehme C., Mouralis D., 2022. 10Be chronology of deglaciation and ice-dammed lake regression in the vicinity of the Mylodon Cave (Cerro Benítez, Patagonia, Chile). *Quat. Sci. Rev*, *278*, 107354.

Glasser N.F., Harrison S., Winchester V., Aniya M., 2004. Late Pleistocene and Holocene palaeoclimate and glacier fluctuations in Patagonia. *Glob. planet. change*, *43*(1-2), 79-101.

Global Network Isotope Precipitation, 2019. Wiser Statistics GNIP Chile Punta Arenas Station. IAEA Nucleus https://www.iaea.org/

Guo W., Zhou C., 2019. Patterns and controls of disequilibrium isotope effects in speleothems: insights from an isotope-enabled diffusion-reaction model and implications for quantitative thermometry. *Geochim. Cosmochim. Acta*, *267*, 196-226.

Hellstrom J., 2003. Rapid and accurate U/Th dating using parallel ion-counting multi-collector ICP-MS. *J. of Analytical Atomic Spectrom.*, *18*(11), 1346-1351.

Hellstrom J., 2006. U–Th dating of speleothems with high initial ^{230}Th using stratigraphical constraint. *Quat. Geochronol.*, *1*(4), 289-295.

Hodell D.A., Kanfoush S.L., Shemesh A., Crosta X., Charles C.D., Guilderson T.P., 2001. Abrupt cooling of Antarctic surface waters & sea ice expansion in the South Atlantic sector of the Southern Ocean at 5000 cal yr BP. *Quat. Res.*, *56*(2), 191-198.

Ivanovic R.F., Gregoire L.J., Burke A., Wickert A.D., Valdes P.J., Ng H.C., Robinson L.F., MacManus J.F., Mitrovica J.X., Lee L., Dentith J.E., 2018. Acceleration of northern ice sheet melt induces AMOC slowdown and northern cooling in simulations of the early last deglaciation. *Paleoceanog. Paleoclim.*, *33*(7), 807-824.

John C.M., Bowen D., 2016. Community software for challenging isotope analysis: First applications of 'Easotope'to clumped isotopes, *Rapid Commun. Mass Spectrom*., 30, 2285-2300.

Kele S., Breitenbach S.F., Capezzuoli E., Meckler A.N., Ziegler M., Millan I.M.,... & Bernasconi S.M., 2015. Temperature dependence of oxygen-and clumped isotope fractionation in carbonates: a study of travertines and tufas in the 6–95°C temperature range. *Geochim. Cosmochim. Acta*, *168*, 172-192.

Kocken I.J., Müller I.A., Ziegler M., 2019. Optimizing the Use of Carbonate Standards to Minimize Uncertainties in Clumped Isotope Data, *Geochem. Geophys. Geosyst*., 20, 5565-5577.

Kluge T., Riechelmann D.F.C., Wieser M., Spötl C., Sültenfuß J., Schröder-Ritzrau A., Niggemann S., Aeschbach-Hertig W., 2010. Dating cave drip water by tritium. *J. of Hydrol.*, *394*(3-4), 396-406.

Kluge T., Affek H.P., Marx T., Aeschbach-Hertig W., Riechelmann D.F.C., Scholz D., ... & Spötl C., 2013. Reconstruction of drip-water $\delta^{18}O$ based on calcite oxygen and clumped isotopes of speleothems from Bunker Cave (Germany). *Clim. Past*, *9*(1), 377-391.

Lachniet M.S., 2009. Climatic and environmental controls on speleothem $\delta^{18}O$ values. *Quat. Sci. Rev*, *28*(5-6), 412-432.

Lamy F., Kaiser J., Arz H.W., Hebbeln D., Ninnemann U., Timm O., ... & Toggweiler J.R., 2007. Modulation of the bipolar seesaw in the S-E Pacific during Termination 1. *Earth Planet. Sci. Lett.*, *259*(3-4), 400-413.

Lamy F., Rühlemann C., Hebbeln D., Wefer G., 2002. High-and low-latitude climate control on the position of the southern Peru-Chile Current during the Holocene. *Paleoceanography*, *17*(2), 16-1.

Lamy F., Kilian R., Arz H.W., Francois J.P., Kaiser J., Prange M., Steinke T., 2010. Holocene changes in the position and intensity of the southern westerly wind belt. *Nature Geoscience*, *3*(10), 695-699.

Lamy F., Arz H.W., Kilian R., Lange C.B., Lembke-Jene L., Wengler M., Kaiser J., Baeza-Urrea O., Hall I.R., Harada N., Tiedemann R., 2015. Glacial reduction and millennial-scale variations in Drake Passage throughflow. *Proc. Natl. Acad. Sci.*, *112*(44), 13496-13501.

Lechleitner, F.A., Amirnezhad-Mozhdehi S., Columbu A., Comas-Bru L., Labuhn I., Pérez-Mejías C., Rehfeld K., 2018. The potential of speleothems from Western Europe as recorders of regional climate: a critical assessment of the SISAL database. *Quaternary*, *1*(3), 30.

Luo X., Rehkämper M., Lee D.C., Halliday A.N., 1997. High precision $^{230}Th/^{232}Th$ and $^{234}U/^{238}U$ measurements using energyfiltered ICP magnetic sector multiple collector mass spectrometry. *Int. J. Mass Spectrom. Ion Processes*, *171*(1-3), 105-117.

Mangini A., Spötl C., Verdes P., 2005. Reconstruction of temperature in the Central Alps during the past 2000 yr from a $\delta^{18}O$ stalagmite record. *Earth Planet. Sci. Lett.*, *235*(3-4), 741-751.

Mansilla C.A., McCulloch R.D., Morello F., 2016. Palaeoenvironmental change in southern Patagonia during Lateglacial & Holocene: implications for forest refugia & climate reconstructions. *Palaeogeogr. Palaeoclimatol. Palaeoecol.*, *447*, 1-11.

Mansilla C.A., McCulloch R.D., Morello F., 2018. The vulnerability of the Nothofagus forest-steppe ecotone to climate change: Palaeoecological evidence from Tierra del Fuego (~ 53 S). *Palaeogeogr. Palaeoclimatol. Palaeoecol.*, *508*, 59-70.

Martin F.M., Todisco D., Rodet J., San Román M., Morello F., Prevosti F., Borrero, L.A., 2015. Nuevas excavaciones en Cueva del Medio: Procesos de formación de la cueva y avances en los estudios de interacción entre cazadores-recolectores y fauna extinta (Pleistoceno Final, Patagonia Meridional). *Magallania (Punta Arenas)*, *43*(1), 165-189.

Martin F.M., Borrero L.A., 2017. Climate change, availability of territory, and Late Pleistocene human exploration of Ultima Esperanza, South Chile. *Quat. Int.*, *428*, 86-95.

Markgraf V., Whitlock C., Haberle S., 2007. Vegetation and fire history during the last 18,000 cal yr BP in Southern Patagonia: Mallín Pollux, Coyhaique, Province Aisén. *Palaeogeogr. Palaeoclimatol. Palaeoecol*, *254*(3-4), 492-507.

Markgraf V., Baumgartner T.R., Bradbury J.P., Diaz H.F., Dunbar R.B., Luckman B.H.,... & Villalba R., 2000. Paleoclimate reconstruction along the Pole–Equator–Pole transect of the Americas (PEP 1). *Quat. Sci. Rev*., *19*(1-5), 125-140.

Matthews A., Affek H.P., Ayalon A., Vonhof H.B., Bar-Matthews M., 2021. Eastern Mediterranean climate change deduced from the Soreq Cave fluid inclusion stable isotopes and carbonate clumped isotopes record of the last 160 ka. *Quat. Sci. Rev.*, *272*, 107223.

McCulloch R.D., Davies S., 2001. Late-glacial and Holocene palaeoenvironmental change in the central strait of magellan, southern Patagonia. *Palaeogeogr. Palaeoclimatol. Palaeoecol.* 173, 143-173.

McCulloch, R.D., Mansilla C.A., Morello F., De Pol-Holz R., San Roman M., Tisdall E., Torres J., 2019. Late glacial and Holocene landscape change and rapid climate and coastal impacts in the Canal Beagle, southernmost Patagonia. *J. of Quat. Sci.*, *34*(8), 674-684.

McCulloch R.D., Blaikie J., Jacob B., Mansilla C.A., Morello F., De Pol-Holz R., San Roman M., Tisdall E., Torres J., 2020. Late glacial and Holocene climate variability, southernmost Patagonia. *Quat. Sci. Rev*. 229, 106131.

McCulloch R.D., Mansilla C.A., Martin F., Borrero L., Staff R.A., Tisdall E.W., 2021. The nature and timing of landscape change at Cerro Benítez, Última Esperanza, southern Patagonia (52°S): New insights into the history of megafaunal extinctions and human occupation. *Quat. Int.*, *601*, 116-129.

McDermott F., 2004. Palaeo-climate reconstruction from stable isotope variations in speleothems: a review. *Quat. Sci. Rev*, *23*(7-8), 901-918.

Meckler A.N., Ziegler M., Millán M.I., Breitenbach S.F.M., Bernasconi S.M., 2014. Long-term performance of the Kiel carbonate device with a new correction scheme for clumped isotope measurements, *Rapid Commun. Mass Spectrom*, 28, 1705-1715.

Miorandi R., Borsato A., Frisia S., Fairchild I.J., Richter D.K., 2010. Epikarst hydrology and implications for stalagmite capture of climate changes at Grotta di Ernesto (NE Italy): results from long-term monitoring. *Hydrol. Proc.*, *24*(21), 3101-3114.

Moreno P.I., 2004. Millennial-scale climate variability in NW Patagonia over the last 15000 yr. *J. Quat. Sci.*, *19*(1), 35-47.

Moreno P.I., François J.P., Villa-Martínez R.P., Moy C.M., 2009. Millennial-scale variability in Southern Hemisphere westerly wind activity over the last 5000 years in SW Patagonia. *Quat. Sci. Rev.*, *28*(1-2), 25-38.

Moreno P.I., Villa-Martínez R., Cárdenas M.L., Sagredo E.A., 2012. Deglacial changes of the southern margin of the southern westerly winds revealed by terrestrial records from SW Patagonia (52 S). *Quat. Sci. Rev*,, *41*, 1-21.

Moreno P.I. and Videla J., 2016. Centennial and millennial-scale hydroclimate changes in northwestern Patagonia since 16,000 yr BP. *Quat. Sci. Rev.*, *149*, 326-337.

Moreno P.I., Videla J., Valero-Garcés B., Alloway B.V., Heusser L.E., 2018a. A continuous record of vegetation, fire-regime and climatic changes in northwestern Patagonia spanning the last 25,000 years. *Quat. Sci. Rev.*, *198*, 15-36.

Moreno P.I., Vilanova I., Villa-Martínez R., Dunbar R.B., Mucciarone D.A., Kaplan M.R., Garreaud R.D., Rojas M., Moy C.M., De Pol-Holz R., Lambert F., 2018b. Onset and evolution of southern annular mode-like changes at centennial timescale. *Sci. Rep.*, *8*(1), 1-9.

Moreno P.I., Simi E., Villa-Martínez R.P., Vilanova I., 2019. Early arboreal colonization, postglacial resilience of deciduous Nothofagus forests, and the SouthWesterly Wind influence in central-east Andean Patagonia. *Quat. Sci. Rev., 218*, 61-74.

Moy C.M., Seltzer G.O., Rodbell D.T., Anderson D. M., 2002. Variability of El Niño/Southern Oscillation activity at millennial timescales during the Holocene epoch. *Nature*, *420*(6912), 162-165.

Mühlinghaus C., Scholz D., Mangini A., 2009. Modelling fractionation of stable isotopes in stalagmites. *Geochim. Cosmochim. Acta, 73*(24), 7275-7289.

Mulvaney R., Abram N.J., Hindmarsh R.C., Arrowsmith C., Fleet L., Triest J.,... & Foord S., 2012. Recent Antarctic Peninsula warming relative to Holocene climate & ice-shelf history. *Nature*, *489*(7414), 141-144.

Nami H.G.n Nakamura T., 1995. Cronología radiocarbónica con AMS sobre muestras de hueso procedentes del sitio Cueva del Medio (Última Esperanza, Chile). In *Anales del Instituto de la Patagonia*.

Nehme C., Kluge T., Verheyden S., Nader F., Charalambidou I., Weissbach T.,... & Claeys P., 2020. Speleothem record from Pentadactylos cave (Cyprus): new insights into climatic variations during MIS 6 and MIS 5 in the Eastern Mediterranean. *Quat. Sci. Rev.*, *250*, 106663.

Petersen S.V., Defliese W.F., Saenger C., Daëron M.,…& Winkelstern I.Z., 2019. Effects of Improved 17O Correction on Interlaboratory Agreement in Clumped Isotope Calibrations, Estimates of Mineral-Specific Offsets, and Temperature Dependence of Acid Digestion Fractionation, *Geochem. Geophys. Geosyst.,* 20, 3495-3519.

Peri P.L., Ladd B., Pepper D.A., Bonser S.P. Laffan S.W. Amelung W., 2012. Carbon ($\delta^{13}C$) and nitrogen (δ^{15} N) stable isotope composition in plant and soil in S outhern P atagonia's native forests. *Glob. Change Biol.*, *18*(1), 311-321.

Prieto A., 1991. Cazadores tempranos y tardíos en Cueva del Lago Sofía 1. *Ans. Inst. Pat. Ser. Cs. Soc.*, *20*, 75-96.

Reimer P.J., Austin W.E., Bard E., Bayliss A., Blackwell P.G., Ramsey C.B., …& Talamo S., 2020. The IntCal20 Northern Hemisphere radiocarbon age calibration curve (0–55 cal kBP). *Radiocarbon*, *62*(4), 725-757.

Romans B.W., Fildani A., Hubbard S.M., Covault J.A., Fosdick J.C., Graham S.A., 2011. Evolution of deep-water stratigraphic architecture, Magallanes Basin, Chile. *Marine Petrol. Geol.*, *28*(3), 612-628

Rozanski K., Araguasaraguas L., Gonfiantini R., 1992: Relationship between long-tenn trends of $\delta^{18}O$ isotope composition of precipitation and climate, *Science*, 258, 981-985.

Sagredo E.A., Moreno P.I., Villa-Martínez R., Kaplan M.R., Kubik P.W., Stern C.R., 2011. Fluctuations of the Última Esperanza ice lobe (52°S), Chilean Patagonia, during the last glacial maximum and T1. *Geomorphology*, *125*(1), 92-108.

Schäbitz F., Wille M., Francois J.P., Haberzettl T., Quintana F., Mayr C., Lucke A., Ohlendorf C., Mancini V., Paez M. M., Prieto R., Zolitschka B., 2013. Reconstruction of palaeoprecipitation based on pollen transfer functions–the record of the last 16 ka from Laguna Potrok Aike, southern Patagonia. *Quat. Sci. Rev., 71*, 175-190.

Schimpf D., Kilian R., Kronz A., Simon K., Spötl C., Wörner G., Deininger M., Mangini A., 2011. The significance of chemical, isotopic, and detrital components in three coeval stalagmites from the superhumid southernmost Andes (53°S) as high-resolution palaeo-climate proxies. *Quat. Sci. Rev., 30*(3-4), 443-459.

Schneider C., Glaser M., Kilian R., Santana A., Butorovic N., Casassa G., 2003. Weather observations across the southern Andes at 53°S. *Phys. Geog.*, *24*(2), 97-119.

Scholz D., Hoffmann D. L., Hellstrom J., Ramsey C.B., 2012. A comparison of different methods for speleothem age modelling. *Quat. Geochronol.*, *14*, 94-104.

Shevenell A.E., Ingalls A.E., Domack E.W., Kelly C., 2011. Holocene Southern Ocean surface temperature variability west of the Antarctic Peninsula. *Nature*, *470*(7333), 250-254.

Sinclair D.J., Banner J.L., Taylor F.W., Partin J., Jenson J., Mylroie J., Goddard E., Quinn T., Jocson J., Miklavič B., 2012. Magnesium and strontium systematics in tropical speleothems from the Western Pacific. *Chem. Geol.*, *294*, 1-17.

Smith G.K., 2021, Calcite straw stalactites growing from concrete structures. *Cave and Karst Science*, 48 (1), 3 – 11

Solari M.A., Hervé F., Le Roux J.P., Airo A., Sial A.N., 2010. Paleoclimatic significance of lacustrine microbialites: a stable isotope case study of two lakes at Torres del Paine, South Chile. *Palaeogeogr. Palaeoclimatol. Palaeoecol.*, *297*(1), 70-82.

Stern C.R., Moreno P.I., Villa-Martínez R., Sagredo E.A., Prieto A., Labarca R., 2011. Evolution of ice-dammed proglacial lakes in Última Esperanza, Chile: implications from the late-glacial R1 eruption of Reclús volcano, Andean Austral Volcanic Zone. *Andean Geol.*, *38*(1), 82-97.

Stuiver M., Polach H.A., 1977. Discussion reporting of ^{14}C data. *Radiocarbon*, *19*(3), 355-363.

Timmermann A., Krebs U., Justino F., Goosse H., Ivanochko T., 2005. Mechanisms for millennial-scale global synchronization during the last glacial period. *Paleoceanography*, *20*(4).

Tremaine D.M., Froelich P.N., Wang Y., 2011. Speleothem calcite farmed in situ: Modern calibration of $\delta^{18}O$ and $\delta^{13}C$ paleoclimate proxies in a continuously-monitored natural cave system. *Geochim. Cosmochim. Acta, 75*(17), 4929-4950.

Toggweiler J.R., Russell J.L., Carson S.R., 2006. Midlatitude westerlies, atmospheric CO_2, and climate change during the ice ages. *Paleoceanography*, *21*(2).

Tonello M.S., Mancini M.V., Seppä H., 2009. Quantitative reconstruction of Holocene precipitation changes in southern Patagonia. *Quat. Res.*, *72*(3), 410-420.

Tuhkanen S., Kuokka I., Hyvönen J., Stenroos S., Niemelä J.,1990. Tierra del Fuego as a target for biogeographical research in the past and present. In *Anales Instituto de la Patagonia* (V 19, Nº. 2, 1-107).

Van Breukelen M.R., Vonhof H.B., Hellstrom J.C., Wester W.C.G., Kroon D., 2008. Fossil dripwater in stalagmites reveals Holocene temperature and rainfall variation in Amazonia. *Earth Planet. Sci. Lett.*, *275*(1-2), 54-60.

Van Geldern R., Barth J.A., 2012. Optimization of instrument setup and post-run corrections for oxygen and hydrogen stable isotope measurements of water by isotope ratio infrared spectroscopy (IRIS). *Limnol. Oceanogr:Methods*,*10*(12),1024-1036.

Van Rampelbergh M., Verheyden S., Allan M., Quinif Y., Keppens E., Claeys P., 2014. Monitoring of a fast-growing speleothem site from the Han-sur-Lesse cave, Belgium, indicates equilibrium deposition of the seasonal $\delta^{18}O$ and $\delta^{13}C$ signals in the calcite. *Clim. Past*, *10*(5), 1871-1885.

Verheyden S., Keppens E., Fairchild I.J., McDermott F., Weis D., 2000. Mg, Sr and Sr isotope geochemistry of a Belgian Holocene speleothem: implications for paleoclimate reconstructions. *Chem. Geol*, *169*(1-2), 131-144.

Villa-Martínez R., Moreno P.I., 2007. Pollen evidence for variations in the southern margin of the westerly winds in SW Patagonia over the last 12,600 years. *Quat. Res.*, *68*(3), 400-409.

Villavicencio N.A., Lindsey E.L., Martin F.M., Borrero L.A., Moreno P.I., Marshall C.R., Barnosky A.D., 2016. Combination of humans, climate, and vegetation change triggered Late Quaternary megafauna extinction in the Última Esperanza region, southern Patagonia, Chile. *Ecography*, *39*(2), 125-140.

971 Wassenburg J.A., Vonhof H.B., Cheng H., Martínez-García A., Ebner P.R., Li X.,...& Haug G.H., 2021. Penultimate
972 deglaciation Asian monsoon response to North Atlantic circulation collapse. *Nature Geoscience*, *14*(12), 937-941.
973 Warken S.F., Schorndorf N., Stinnesbeck W., Hennhoefer D., Stinnesbeck S.R., Förstel J.,... & Frank N., 2021. Solar forcing
974 of early Holocene droughts on the Yucatán peninsula. *Scientific Reports*, *11*(1), 1-12.
975 Weiss divide project members, 2013. Onset of deglacial warming in West Antarctica driven by local orbital forcing. *Nature*,
976 500, 440-444.
977 Uemura R., Kina Y., Shen C.C., Omine K., 2020. Experimental evaluation of oxygen isotopic exchange between inclusion
978 water and host calcite in speleothems. *Clim. Past*, *16*(1), 17-27.
979 Zolitschka B., Fey M., Janssen S., Maidana N.I., Mayr C., Wulf S., Haberzettle T., Corbella H;, Lucke A;, Ohlendorf C.,
980 Schäbitz F., 2019. Southern Hemispheric westerlies control sedimentary processes of Laguna Azul (SE Patagonia,
981 Argentina). *The Holocene*, *29*(3), 403-420.